Cell

Article

Circuit mechanism for suppression of frontal cortical ignition during NREM sleep

Graphical abstract

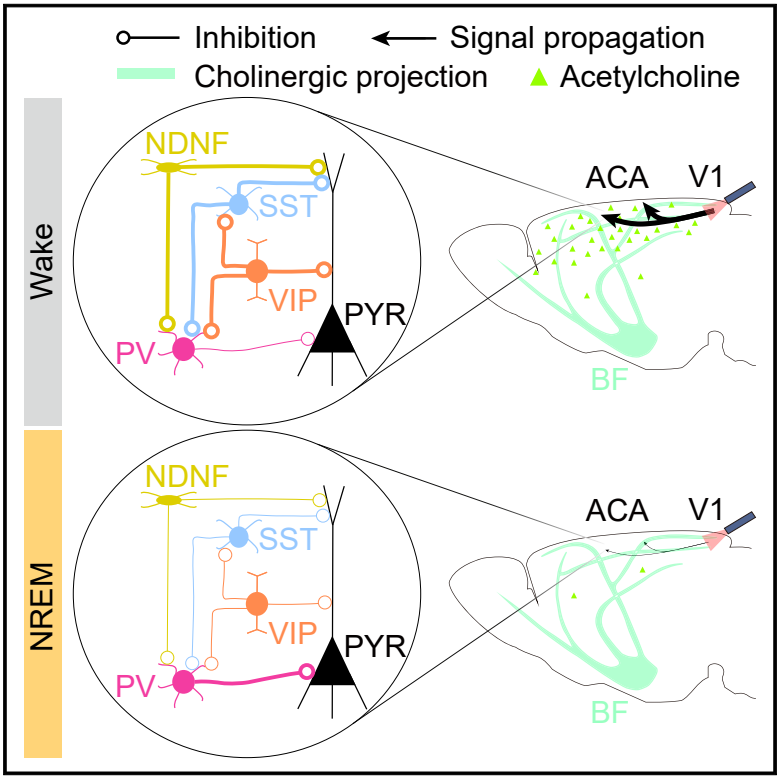

Authors

Bing Li, Chenyan Ma, Yun-An Huang, ..., Gabriel Montaldo, Alan Urban, Yang Dan

Correspondence

ydan@berkeley.edu

In brief

Investigation into the circuit mechanisms that diminish awareness during sleep shows that frontal cortical ignition is suppressed during NREM sleep due to reduced cholinergic modulation and a shift from dendritic to perisomatic inhibition of frontal cortical pyramidal neurons.

Highlights

- Visual-to-frontal cortex activity propagation is strongly reduced during NREM sleep
- Responses of frontal pyramidal neurons are strongly inhibited during NREM sleep
- Basal forebrain cholinergic neurons powerfully modulate frontal cortical ignition
- Increased perisomatic inhibition during NREM sleep suppresses cortical ignition

Li et al., 2023, Cell *186*, 5739–5750
December 21, 2023
https://doi.org/10.1016/j.cell.2023.11.012

CellPress

Cell

CellPress
OPEN ACCESS

Article

Circuit mechanism for suppression of frontal cortical ignition during NREM sleep

Bing Li,[1,3] Chenyan Ma,[1,3] Yun-An Huang,[2] Xinlu Ding,[1] Daniel Silverman,[1] Changwan Chen,[1] Dana Darmohray,[1] Lihui Lu,[1] Siqi Liu,[1,4] Gabriel Montaldo,[2] Alan Urban,[2] and Yang Dan[1,5,*]

[1]Division of Neurobiology, Department of Molecular and Cell Biology, Helen Wills Neuroscience Institute, Howard Hughes Medical Institute, University of California, Berkeley, Berkeley, CA 94720, USA

[2]Neuro-Electronics Research Flanders, VIB, Department of Neurosciences, KU Leuven, imec, Leuven, Belgium

[3]These authors contributed equally

[4]Present address: Department of Life Science, Faculty of Science, The Chinese University of Hong Kong, Hong Kong, China

[5]Lead contact

*Correspondence: ydan@berkeley.edu

https://doi.org/10.1016/j.cell.2023.11.012

SUMMARY

Conscious perception is greatly diminished during sleep, but the underlying circuit mechanism is poorly understood. We show that cortical ignition—a brain process shown to be associated with conscious awareness in humans and non-human primates—is strongly suppressed during non-rapid-eye-movement (NREM) sleep in mice due to reduced cholinergic modulation and rapid inhibition of cortical responses. Brain-wide functional ultrasound imaging and cell-type-specific calcium imaging combined with optogenetics showed that activity propagation from visual to frontal cortex is markedly reduced during NREM sleep due to strong inhibition of frontal pyramidal neurons. Chemogenetic activation and inactivation of basal forebrain cholinergic neurons powerfully increased and decreased visual-to-frontal activity propagation, respectively. Furthermore, although multiple subtypes of dendrite-targeting GABAergic interneurons in the frontal cortex are more active during wakefulness, soma-targeting parvalbumin-expressing interneurons are more active during sleep. Chemogenetic manipulation of parvalbumin interneurons showed that sleep/wake-dependent cortical ignition is strongly modulated by perisomatic inhibition of pyramidal neurons.

INTRODUCTION

In daily life, we are constantly bombarded by sensory stimuli from multiple modalities, but most of them do not reach our conscious awareness. Although even subliminal stimuli can activate sensory cortices, conscious awareness depends on the propagation of the neuronal activity to a large brain network (the "global neuronal workspace") that includes parietal and frontal areas,[1,2] and these areas further amplify the activity through recurrent excitation, and this process is referred to as "global ignition."[3] Global ignition in the context of conscious awareness has been studied primarily in humans[3] and recently in non-human primates.[2] However, dissecting the underlying circuit mechanism, especially at the level of genetically defined cell types, remains difficult.

The level of conscious awareness changes profoundly at sleep-wake transitions on a daily basis,[4] but the underlying mechanism is not well understood. In the visual system, eyelid closure and pupil constriction during sleep can affect retinal responses to visual stimuli,[5] and altered gating by the thalamus (TH) may further attenuate the responses in the visual cortex.[6] In addition, effective connectivity between cortical areas measured by responses to transcranial magnetic stimulation is reduced during sleep.[7] Interestingly, with auditory stimulation, sleep has little effect on response magnitudes in early auditory cortices but strongly attenuates responses in downstream association areas and feedback processing.[8,9] This suggests that sleep preferentially suppresses sensory activation of higher cortical areas.

In this study, we measured sleep/wake-dependent cortical ignition in mice, an animal model that allows dissection of neural circuits at the level of genetically defined cell types. We focused on activity propagation from the visual cortex (V1) to other brain regions, especially the frontal cortex, as this propagation has been linked to conscious detection of visual stimuli.[2] Since sleep is associated with multiple changes that affect V1 responses to visual stimuli, including pupil constriction[5] and thalamic gating,[6] we bypassed the early visual pathway and used direct optogenetic stimulation to activate V1 pyramidal neurons. To measure activity propagation, we used two imaging techniques with complementary features: functional ultrasound imaging (fUSi) of hemodynamic responses[10–12] for brain-wide mapping of activity propagation, and calcium imaging for measuring the activity of specific cortical cell types. We found that activity propagation

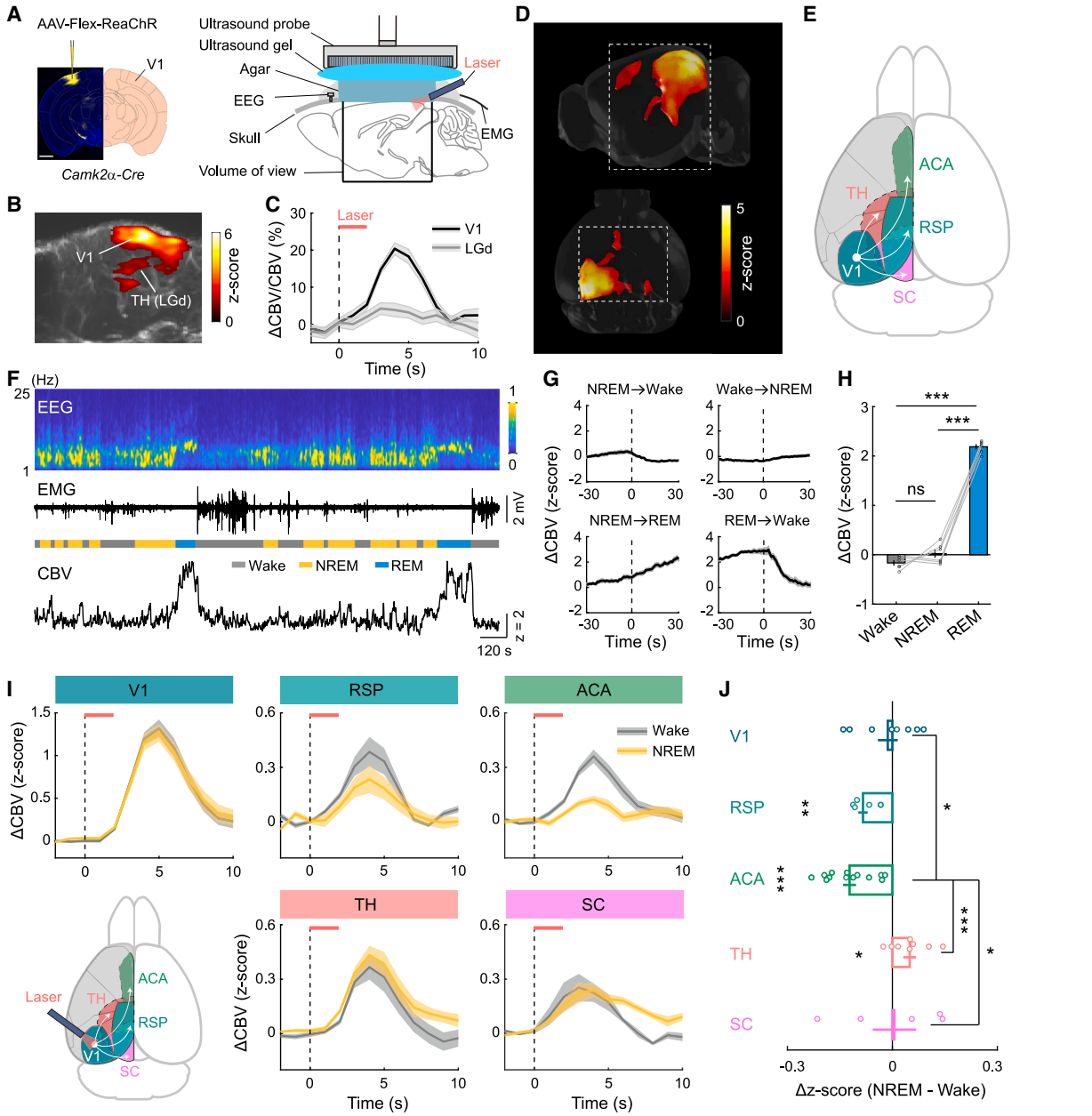

Figure 1. Functional ultrasound imaging of brain-wide CBV responses to optogenetic V1 activation during sleep and wakefulness

(A) Schematic showing virus injection and expression in V1 (left; scale bars, 1 mm) and functional ultrasound imaging with optogenetic V1 stimulation and EEG/EMG recordings (right). Black box, volume of view.

(B) Typical imaging session (sagittal section) showing regions significantly activated by V1 stimulation (n = 17 trials). Activity in each voxel was z-scored and color coded. Sampling frequency, 1 Hz. LGd, dorsal lateral geniculate complex of the thalamus.

(C) CBV responses in V1 and LGd.

(D) Brain-wide responses averaged across mice. Dashed boxes, volume of view.

(E) Summary of main brain regions activated by V1 stimulation. Dashed lines outline brain regions below cortical surface.

(F) EEG power spectrogram (recorded over the frontal cortical area), EMG, and brain-wide CBV activity (bottom) in an example session with multiple sleep and wake episodes (color coded).

(G) Mean brain-wide CBV activity at brain-state transitions. Time 0 indicates transition point.

(H) Mean brain-wide CBV activity in each brain state. Each line represents data from one mouse.

(I) V1-evoked CBV responses during NREM sleep and wakefulness averaged across all mice. Baseline signal was subtracted for each trial before averaging. Horizontal red bar, laser stimulation.

(legend continued on next page)

from V1 to other cortical areas—especially the anterior cingulate area (ACA) of the frontal cortex—is markedly reduced during non-rapid-eye-movement (NREM) sleep. V1 activation during NREM sleep, but not wakefulness, evoked a strong inhibition of ACA pyramidal neurons. Chemogenetic activation and inactivation of basal forebrain cholinergic neurons, which are active during wakefulness but not NREM sleep,[13,14] strongly increased and decreased V1-to-ACA activity propagation, respectively. Cell-type-specific calcium imaging showed that vasoactive intestinal peptide (VIP)-, somatostatin (SST)-, and neuron-derived neurotrophic factor (NDNF)-expressing GABAergic interneurons, all of which preferentially target pyramidal neuron dendrites,[15–18] are more active during wakefulness. By contrast, soma-targeting parvalbumin (PV)-expressing neurons are more active during NREM sleep. Bidirectional chemogenetic manipulation of ACA PV neurons demonstrates their substantial contribution to V1-evoked inhibition of pyramidal neurons during NREM sleep. Thus, sleep/wake-dependent cortical ignition is strongly modulated by cholinergic activity together with a shift in the balance between dendritic and perisomatic inhibition of cortical pyramidal neurons.

RESULTS

Brain-wide fUSi of activity propagation

To activate V1 pyramidal neurons optogenetically, we injected adeno-associated virus (AAV) with Cre-inducible expression of red-activatable channelrhodopsin (ReaChR)[19] (AAV2-Flex-ReaChR-mCitrine) into V1 of *Camk2α-Cre* mice. A brief laser stimulation (635 nm, 10–20 mW, 2 s) was applied in V1, and responses were measured over a large portion of the mouse brain using fUSi[10–12,20] (Figure 1A, ~180 trials/session, 2–3 sessions/mouse). fUSi measures Doppler spectrum intensity, which is proportional to cerebral blood volume (CBV). When a brain region is activated, local blood vessels dilate, resulting in an increased CBV.[21] In addition to V1, we observed robust CBV responses in several cortical areas such as the retrosplenial cortex (RSP) and the ACA of the frontal cortex (Figures 1B–1E and S1A; Video S1; n = 10 mice for brain-wide responses in Figure 1D), which are known to receive excitatory projections from V1.[22] Subcortical regions such as the TH and superior colliculus (SC) were also reliably activated. This provided a brain-wide view of the main activity propagation from V1 pyramidal neurons. Of course, besides the areas described above, neurons in other brain regions may also respond to V1 stimulation, but the associated CBV activity was below the threshold for detection.

Cortical ignition is suppressed during NREM sleep

After extensive habituation under the head-fixed condition,[5] mice routinely underwent multiple sleep-wake cycles during each imaging session (Figure 1F; Data S1), allowing us to compare the activity across brain states. Wake, NREM, and rapid eye movement (REM) sleep were classified based on electroencephalogram (EEG) and electromyogram (EMG) recordings. Brain-wide CBV activity measured with fUSi was comparable between NREM sleep and wakefulness (mostly quiet wakefulness under the head-fixed condition) but significantly higher during REM sleep (Figures 1F–1H; wake vs. NREM, $p = 0.12$; wake vs. REM, $p < 10^{-8}$; NREM vs. REM, $p < 10^{-8}$; n = 6 mice, one-way ANOVA with post hoc Tukey's test), consistent with previous observations.[23]

With the 2-s laser stimulation, which caused no significant change in sleep-wake brain states (Figures S1C and S1D; wake, $p = 0.44$; NREM, $p = 0.36$; REM, $p = 0.31$; n = 8 mice, bootstrap) or motor activity (Figures S1E and S1F), the CBV response in V1 was similar during NREM sleep and wakefulness (Figures 1I and 1J; $p = 0.68$, n = 8 mice, two-tailed paired t test), likely because V1 activity was dominated by direct optogenetic activation. However, in the RSP and ACA, the responses were significantly weaker during NREM sleep (RSP, $p = 0.0051$, n = 5 mice; ACA, $p = 0.000038$, n = 13 mice), indicating reduced activity propagation from V1 to higher cortical areas. Interestingly, we found no response reduction in the SC ($p = 0.94$, n = 5 mice) and a slight increase in the TH ($p = 0.039$, n = 8 mice). This suggests that NREM sleep preferentially suppresses activity propagation within the cortex, although it is possible that activity suppression in some small subcortical regions (e.g., particular thalamic nuclei) was undetected by fUSi. During REM sleep, activity propagation in the cortex was also stronger than during NREM sleep (Figure S2A). However, due to the general paucity of REM sleep and hence the small number of laser trials in this state, the measurement was much less reliable and therefore not considered further in this study.

Rapid inhibition of ACA pyramidal neurons during NREM sleep

To determine whether the reduced CBV response during NREM sleep reflects reduced neuronal spiking or other changes affecting hemodynamic activity, we next measured V1-evoked responses with fiber photometry calcium imaging. Outside of V1, we focused on the frontal region ACA, which showed the most significant reduction of CBV response during NREM sleep (Figures 1I and 1J).

AAV9-CaMKIIα-GCaMP6s was injected into V1 and ACA to label pyramidal neurons (Figures S2D–S2F), and fiber photometry was used to measure their calcium activity in freely moving mice (Figure 2A). The ongoing activity of both V1 and ACA pyramidal neurons was higher during wakefulness and REM sleep than NREM sleep (Figures 2B–2D; in V1, wake vs. NREM, $p < 10^{-6}$; wake vs. REM, $p = 0.75$; NREM vs. REM, $p < 10^{-6}$; in ACA, wake vs. NREM, $p < 10^{-4}$; wake vs. REM, $p < 10^{-5}$; NREM vs. REM, $p < 10^{-6}$; n = 8 mice, one-way ANOVA with post hoc Tukey's test). We then measured the responses to V1 stimulation in each brain state (Figures 2E, 2F, S1B, and S2C). V1 neurons

(J) Difference in response amplitudes between NREM sleep and wakefulness. Each data point represents one mouse. Comparison within each region: V1, $p = 0.68$; RSP, $p = 0.0051$; ACA, $p = 0.000038$; TH, $p = 0.039$; SC, $p = 0.94$ (two-tailed paired t test). Comparison between regions: V1 vs. ACA, $p = 0.044$; ACA vs. TH, $p = 0.00048$; ACA vs. SC, $p = 0.043$ (one-way ANOVA with post hoc Tukey's test).
Bar and error bars, mean ± SEM. Shading, ±SEM. *$p < 0.05$; **$p < 0.01$; ***$p < 0.001$; ns, not significant.
See also Figures S1 and S2.

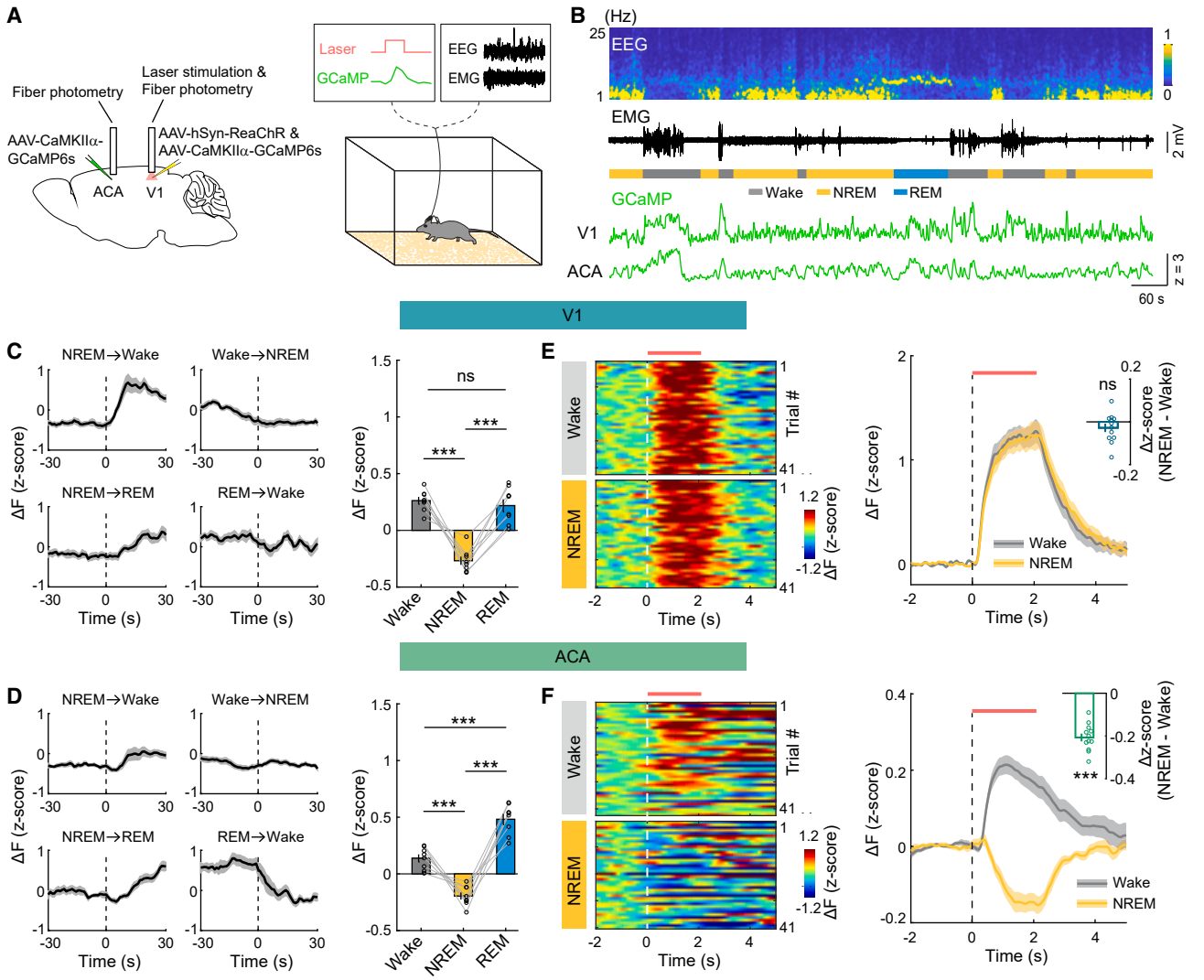

Figure 2. Calcium imaging of ACA and V1 pyramidal neuron responses to optogenetic V1 activation

(A) (Left) Schematic of virus injection for calcium imaging of V1-evoked ACA and V1 pyramidal neuron activity. (Right) Schematic of fiber photometry imaging in freely moving mice.

(B) An example session with EEG (recorded over the frontal cortical area), EMG, and calcium activity in V1 and ACA.

(C) (Left) Mean V1 calcium activity at brain-state transitions. Time 0 indicates transition point. (Right) Mean V1 calcium activity in each brain state. Each line represents one mouse.

(D) Similar to (C), but for ACA pyramidal neuron calcium activity.

(E) (Left) V1 pyramidal neuron calcium activity evoked by optogenetic stimulation in an example session, with trials during wakefulness and NREM sleep. Horizontal red bar, laser stimulation. (Right) Optogenetically evoked V1 activity averaged across mice. Inset, difference in averaged response amplitudes between NREM sleep and wakefulness for each mouse. Baseline signal was subtracted for each trial before averaging.

(F) Similar to (E), but for V1-evoked ACA pyramidal neuron calcium activity.

Bar and error bar, mean ± SEM. Shading, ±SEM. *p < 0.05; **p < 0.01; ***p < 0.001; ns, not significant.

See also Figures S1 and S2.

were strongly activated by laser stimulation, with no significant difference in the response amplitude between wakefulness and NREM sleep (Figure 2E; p = 0.18, n = 12 mice, two-tailed paired t test). However, the responses in the ACA showed striking differences: ACA pyramidal neurons exhibited a strong excitation during wakefulness but a robust inhibition during NREM sleep, with the activity dropping below the baseline level (Figure 2F; $p < 10^{-6}$, n = 12 mice, two-tailed paired t test). These observations were confirmed by two-photon imaging of ACA pyramidal neurons in *Vglut1-Cre* mice (Figures S2G–S2K). Thus, in addition to the CBV responses measured with fUSi (Figures 1I and 1J), calcium responses of ACA pyramidal neurons also depend on brain states. Furthermore, they point to an important role of cortical inhibition in gating ignition, as the rapid suppression

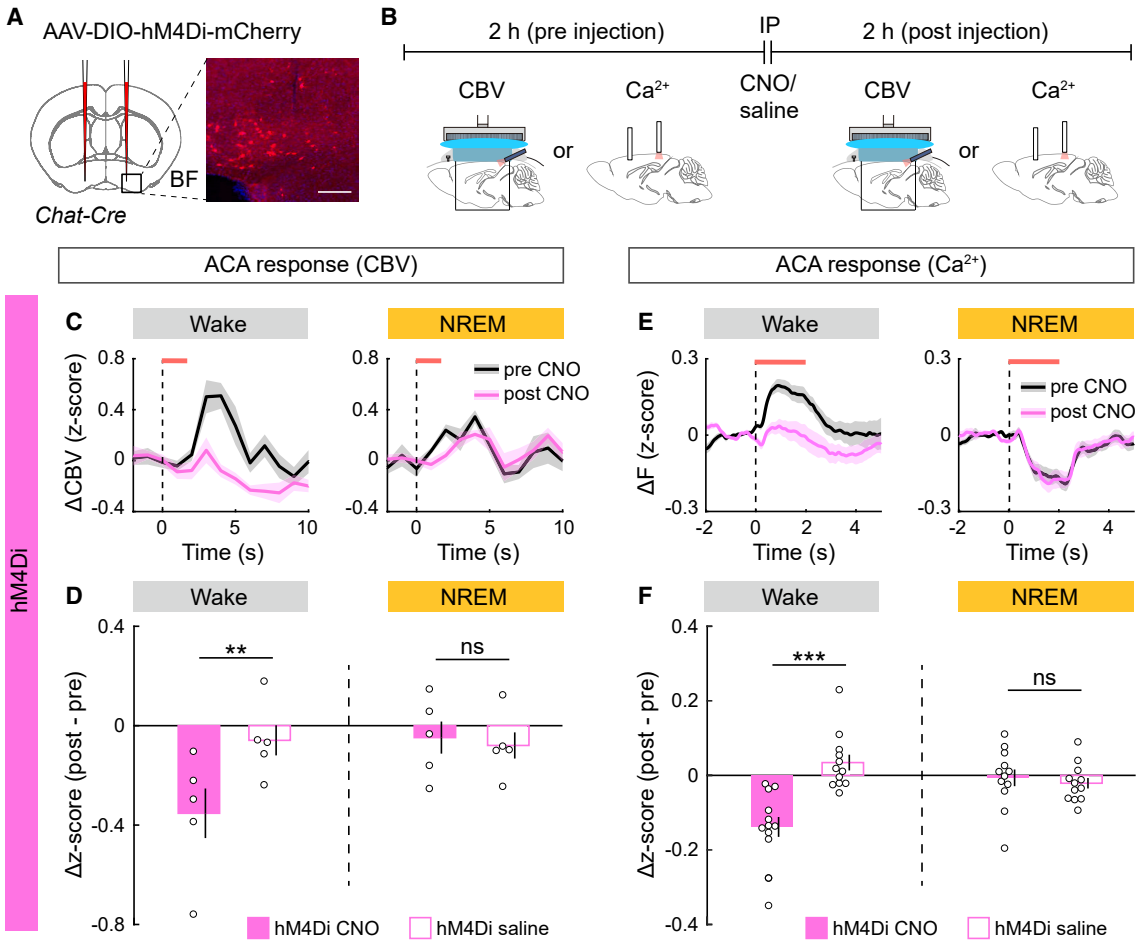

Figure 3. Effects of chemogenetic inactivation of basal forebrain cholinergic neurons on V1-to-ACA activity propagation

(A) Virus injection and expression in basal forebrain (BF) cholinergic neurons. Scale bars, 200 μm.

(B) Schematic for experimental session with chemogenetic inactivation. IP, intraperitoneal injection.

(C) V1-evoked ACA CBV responses before (black) and after (colored) CNO injection during wakefulness (left) or NREM sleep (right), averaged across mice expressing hM4Di in cholinergic neurons. Baseline signal was subtracted for each trial before averaging. Horizontal red bar, laser stimulation.

(D) Summary of amplitude difference before and after CNO (filled) or saline (open) injection. Each point represents one mouse.

(E and F) Similar to (C) and (D), but for ACA pyramidal neuron calcium activity.

Bar and error bar, mean ± SEM. Shading, ±SEM. *$p < 0.05$; **$p < 0.01$; ***$p < 0.001$; ns, not significant.

See also Figures S3 and S5.

of ACA pyramidal neurons may effectively prevent activity amplification through recurrent excitation, which can give rise to late components of sensory responses that are indicative of conscious perception.[4,24]

Cholinergic modulation of cortical ignition

What mechanism underlies the brain-state dependence of activity propagation in the cortex? An important neuromodulatory system regulating brain arousal and conscious experience originates from the basal forebrain cholinergic neurons,[25] which project extensively to the cortex[26] and are active during wakefulness but quiescent during NREM sleep.[13,14] A previous study also showed that cholinergic stimulation of the prefrontal cortex is sufficient to restore wake-like behavior in rats under anesthesia.[27] Although other neuromodulatory systems (e.g., noradrenergic neurons in the locus coeruleus) also project to the cortex and are more active during wakefulness than NREM sleep, we noticed that the V1-to-ACA activity propagation was stronger during REM sleep than NREM sleep as well (Figures S2A and S2B). Whereas cholinergic neurons are active during both wakefulness and REM sleep,[13,14] noradrenergic neurons are completely inactive during REM sleep,[28] suggesting that their activity is not required for increased V1-to-ACA activity propagation. We thus tested the causal role of basal forebrain cholinergic neurons through chemogenetic manipulation using designer receptors exclusively activated by designer drugs (DREADD).[29]

First, we inactivated the cholinergic neurons by injecting AAV2-DIO-hM4Di-mCherry into the basal forebrain of *Chat-Cre* mice (Figure 3A); CBV and calcium responses to V1 stimulation

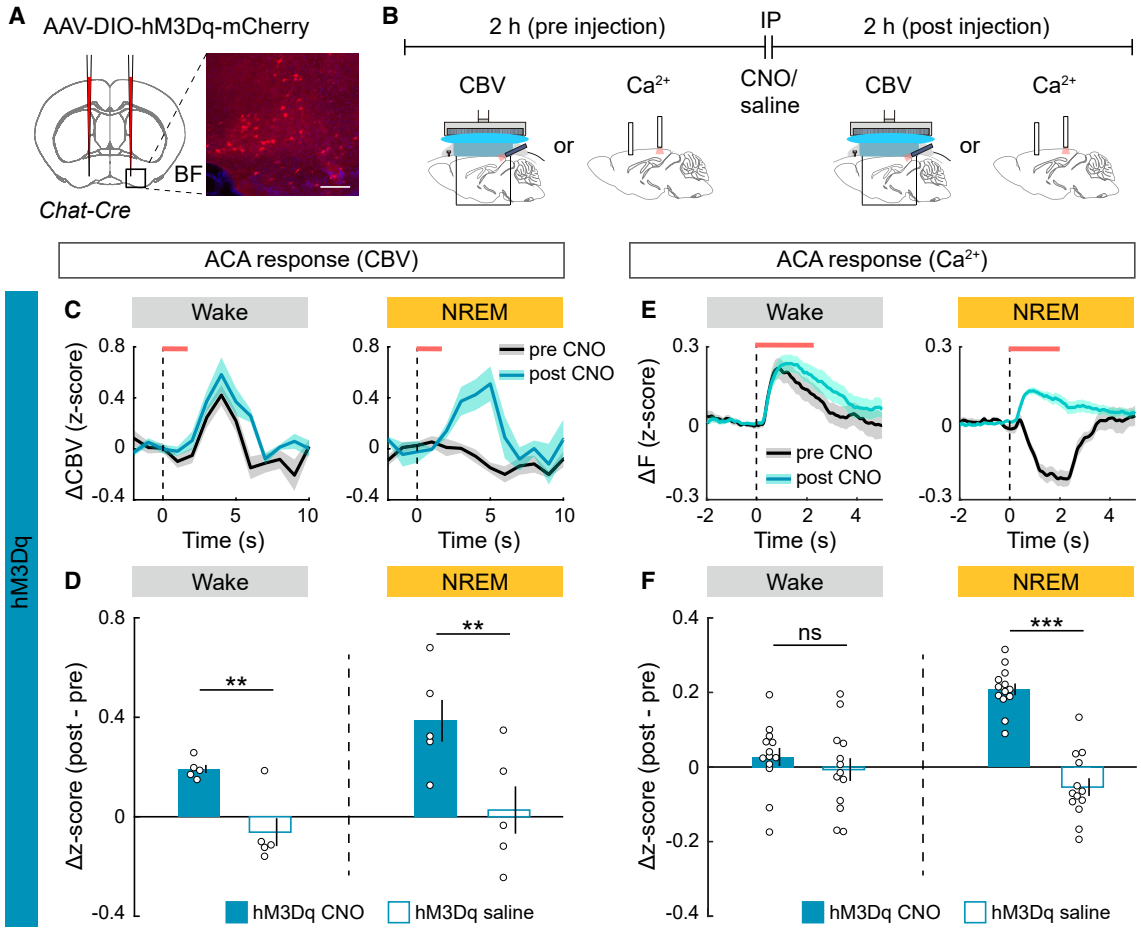

Figure 4. Effects of chemogenetic activation of basal forebrain cholinergic neurons on V1-to-ACA activity propagation

(A) Virus injection and expression in basal forebrain cholinergic neurons. Scale bars, 200 μm.

(B) Schematic for experimental session with chemogenetic activation.

(C) V1-evoked ACA CBV responses before (black) and after (colored) CNO injection during wakefulness (left) or NREM sleep (right), averaged across mice expressing hM3Dq in cholinergic neurons. Baseline signal was subtracted for each trial before averaging. Horizontal red bar, laser stimulation.

(D) Summary of amplitude difference before and after CNO (filled) or saline (open) injection. Each point represents one mouse.

(E and F) Similar to (C) and (D), but for ACA pyramidal neuron calcium activity.

Bar and error bar, mean ± SEM. Shading, ±SEM. *p < 0.05; **p < 0.01; ***p < 0.001; ns, not significant.

See also Figures S4 and S5.

were measured both before and after clozapine N-oxide (CNO) injection (1 mg/kg, Figure 3B). CNO-induced cholinergic inactivation caused a slight decrease in wakefulness and increase in NREM sleep, but within each brain state, the EEG power spectrum showed no change (Figures S3A and S3B). When V1-evoked CBV response in the ACA was compared before and after CNO injection within the same brain state, we found a substantial decrease for laser trials presented during wakefulness but not during NREM sleep (Figure 3C). In the control experiment saline injection caused no significant change in the CBV response (Figure S3C), and the difference between the responses before and after injection was significantly larger for CNO than saline during wakefulness (Figure 3D; wake, p = 0.01; NREM, p = 0.57; n = 5 mice, two-tailed paired t test). Calcium imaging from ACA pyramidal neurons also showed a strong CNO-induced decrease in V1-evoked response during wakefulness but not NREM sleep (Figures 3E, 3F, and S3D; in 3F, wake, p = 0.00016; NREM, p = 0.61; n = 12 mice, two-tailed paired t test), consistent with the observation using fUSi. The lack of effect of chemogenetic inactivation during NREM sleep is likely because basal forebrain cholinergic neurons are naturally inactive during NREM sleep.[13,14] Notably, even during wakefulness, CNO had no significant effect on laser-induced activation of V1 neurons (Figures S3E and S3F; wake, p = 0.37; NREM, p = 0.78; n = 6 mice, two-tailed paired t test), indicating that the reduction of ACA response is caused by suppressed activity propagation outside of V1.

We then tested the effect of cholinergic activation by injecting AAV2-DIO-hM3Dq-mCherry into the basal forebrain of *Chat-Cre* mice (Figures 4A and 4B). CNO injection caused significant

increases in both CBV and calcium responses of the ACA, especially during NREM sleep (Figures 4C–4F and S4E–S4H; in 4D, wake, $p = 0.0059$; NREM, $p = 0.0065$; $n = 5$ mice; in 4F, wake, $p = 0.51$; NREM, $p < 10^{-5}$; $n = 13$ mice; in S4H, wake, $p = 0.25$; NREM, $p = 0.22$; $n = 6$ mice; two-tailed paired t test), opposite to the effect of hM4Di-mediated cholinergic inactivation. Besides an increase in wakefulness and decrease in NREM sleep (Figure S4A), CNO-induced cholinergic activation reduced EEG delta power across brain states (Figure S4B), consistent with a previous report.[30] When we selected subsets of laser trials before and after CNO injection with matched delta power, we still found enhanced CBV and calcium responses during NREM sleep (Figures S4C and S4D; CBV response, $p = 0.035$, $n = 5$ mice; calcium response, $p = 0.0035$, $n = 13$ mice; two-tailed paired t test), indicating that the increase in V1-to-ACA activity propagation is partially dissociable from the decrease in EEG delta activity.

To further ensure that the effect of cholinergic modulation on cortical ignition is not due to a change in overall arousal, we performed local chemogenetic manipulation of cholinergic input to the ACA (Figures S5A and S5B). Activation or inactivation of cholinergic input through local CNO infusion in the ACA caused no significant change in sleep-wake brain states or EEG power spectrum (Figures S5C, S5D, S5G, and S5H). However, local inactivation significantly decreased ACA pyramidal neuron responses during wakefulness (Figures S5E and S5F; wake, $p = 0.0034$; NREM, $p = 0.28$; $n = 6$ mice, two-tailed paired t test), whereas local activation enhanced ACA responses during NREM sleep (Figures S5I and S5J; wake, $p = 0.79$; NREM, $p = 0.021$; $n = 7$ mice, two-tailed paired t test).

Notably, calcium imaging showed that basal forebrain cholinergic neuron activation largely eliminated the V1-evoked inhibition of ACA pyramidal neurons during NREM sleep and converted the response to an overall excitation (Figure 4E, right plot). This suggests that the effect of cholinergic modulation is partly mediated by changes in inhibitory inputs. Indeed, neural network modeling showed that inhibitory inputs to pyramidal neurons could powerfully regulate inter-areal activity propagation in the cortex.[31,32]

Roles of VIP, SST, NDNF, and PV GABAergic interneurons

We next investigated the source of inhibition that is important for the suppression of cortical ignition during NREM sleep. Previous studies have shown that VIP-, SST-, NDNF-, and PV-expressing inhibitory interneurons exhibit different responses to cholinergic modulation, and their activity exerts distinct impacts on cortical pyramidal neurons.[15–18,33–37] As a first step to assess the functional contribution of each interneuron subtype to V1-evoked inhibition of pyramidal neurons during NREM sleep, we performed fiber photometry calcium imaging after injecting AAV9-Flex-GCaMP6s into the ACA of *Vip*-, *Sst*-, *Ndnf*-, or *Pvalb-Cre* mice.[38–41]

We found that VIP, SST, and NDNF neurons all showed higher ongoing activity during wakefulness than NREM sleep (Figures 5A, 5C, and 5E; VIP neurons, wake vs. NREM, $p = 0.00012$; wake vs. REM, $p = 0.28$; NREM vs. REM, $p < 10^{-5}$; $n = 7$ mice; SST neurons, wake vs. NREM, $p < 10^{-5}$; wake vs. REM, $p = 0.00017$; NREM vs. REM, $p = 0.042$; $n = 6$ mice; NDNF neurons, wake vs. NREM, $p = 0.028$; wake vs. REM, $p < 10^{-6}$; NREM vs. REM, $p < 10^{-6}$; $n = 5$ mice; one-way ANOVA with post hoc Tukey's test). However, PV neurons were significantly more active during NREM sleep (Figure 5G; wake vs. NREM, $p = 0.0017$; wake vs. REM, $p < 10^{-9}$; NREM vs. REM, $p < 10^{-9}$; $n = 8$ mice, one-way ANOVA with post hoc Tukey's test), similar to that found in the somatosensory cortex.[42,43] Upon V1 stimulation, ACA VIP and SST neurons were excited during wakefulness but showed no response or reduced activity during NREM sleep (Figures 5B and 5D), making them unlikely to be the sources of V1-evoked rapid inhibition of pyramidal neurons (Figure 2F). Only PV and NDNF neurons exhibited transient excitation during NREM sleep (Figures 5F and 5H), which could contribute to the inhibition of ACA pyramidal neurons.

To test the causal roles of PV and NDNF neuron activity in pyramidal neuron inhibition, we performed chemogenetic activation or inactivation after injecting AAV2-DIO-hM3Dq-mCherry or AAV2-DIO-hM4Di-mCherry, respectively, into the ACA (Figures 6A and S6). CNO-induced activation of PV neurons in *Pvalb-Cre* mice reduced V1-evoked excitation of ACA pyramidal neurons during wakefulness but not NREM sleep (Figures 6B and 6C; wake, hM3Dq CNO vs. hM3Dq saline, $p = 0.027$; NREM, hM3Dq CNO vs. hM3Dq saline, $p = 0.57$; $n = 6$ mice, two-tailed paired t test), whereas activating NDNF neurons in *Ndnf-Cre* mice had no significant effect (Figures S6H and S6I; wake, $p = 0.56$; NREM, $p = 0.53$; $n = 5$ mice, two-tailed paired t test). Furthermore, hM4Di-mediated inactivation of PV neurons, but not NDNF neurons, markedly reduced V1-evoked inhibition of pyramidal neurons during NREM sleep (Figures 6B, 6C, S6J, and S6K; in Figure 6C, wake, hM4Di CNO vs. hM4Di saline, $p = 0.64$; NREM, hM4Di CNO vs. hM4Di saline, $p = 0.032$; $n = 5$ mice; in Figure S6K, wake, $p = 0.016$; NREM, $p = 0.77$; $n = 6$ mice; two-tailed paired t test). These results suggest that PV but not NDNF neurons contribute strongly to the inhibition of pyramidal neuron responses during NREM sleep. Interestingly, during wakefulness, NDNF neuron inactivation slightly reduced the excitation of pyramidal neurons (Figures S6J and S6K). This may be caused by a reduction of their inhibition of PV neurons,[17,37] which could lead to a stronger suppression of pyramidal neurons (Figures 6B and 6C).

DISCUSSION

Combining fUSi and calcium imaging with optogenetic stimulation in mice, we have shown that activity propagation from V1 to higher cortical areas is strongly suppressed during NREM sleep (Figures 1 and 2), reminiscent of the reduced effective connectivity between cortical areas during human NREM sleep, as measured by EEG and transcranial magnetic stimulation.[7] Outside of V1, the activation of cortical, but not subcortical, areas was reduced during NREM sleep, suggesting that cortico-cortical communication is particularly sensitive to brain-state changes. We note that although both fUSi and calcium imaging showed suppression of V1-to-ACA activity propagation during NREM sleep, there are notable differences between the two techniques: CBV signals showed a weaker increase

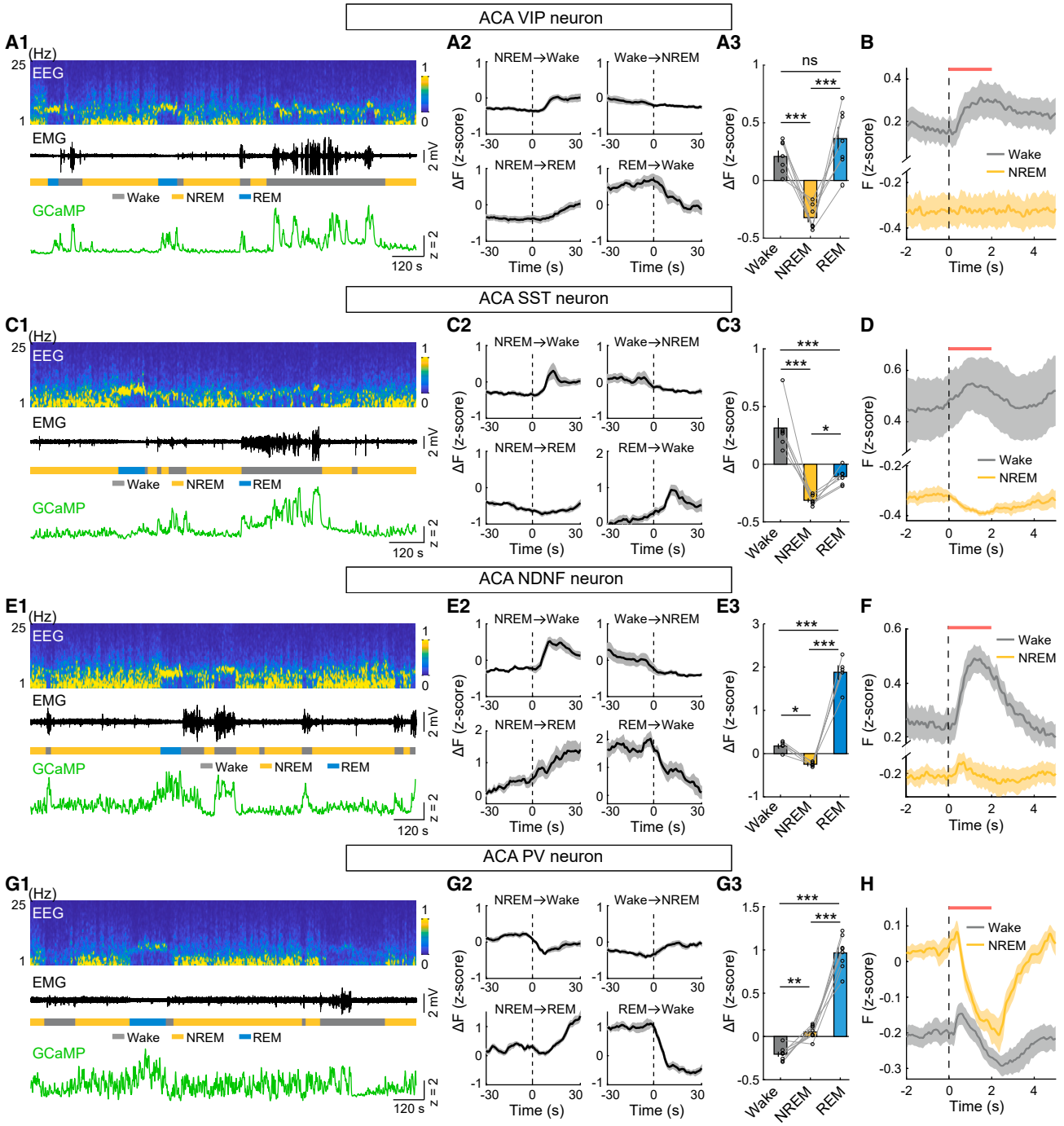

Figure 5. Brain-state-dependent activity of VIP, SST, NDNF, and PV GABAergic interneurons

(A) ACA VIP neuron calcium activity. (A1) An example session with EEG (recorded over the frontal cortical area), EMG, and calcium imaging from ACA VIP neurons. (A2) Mean VIP neuron calcium activity at brain-state transitions. Time 0 indicates transition point. (A3) Mean ACA VIP neuron calcium activity in each brain state. Each line represents one mouse.

(B) Average V1-evoked activity of ACA VIP neurons. Horizontal red bar, laser stimulation.

(C and D) Similar to (A) and (B), but for ACA SST neurons.

(E and F) Similar to (A) and (B), but for ACA NDNF neurons.

(G and H) Similar to (A) and (B), but for ACA PV neurons.

Bar and error bar, mean ± SEM. Shading, ±SEM. *$p < 0.05$; **$p < 0.01$; ***$p < 0.001$; ns, not significant.

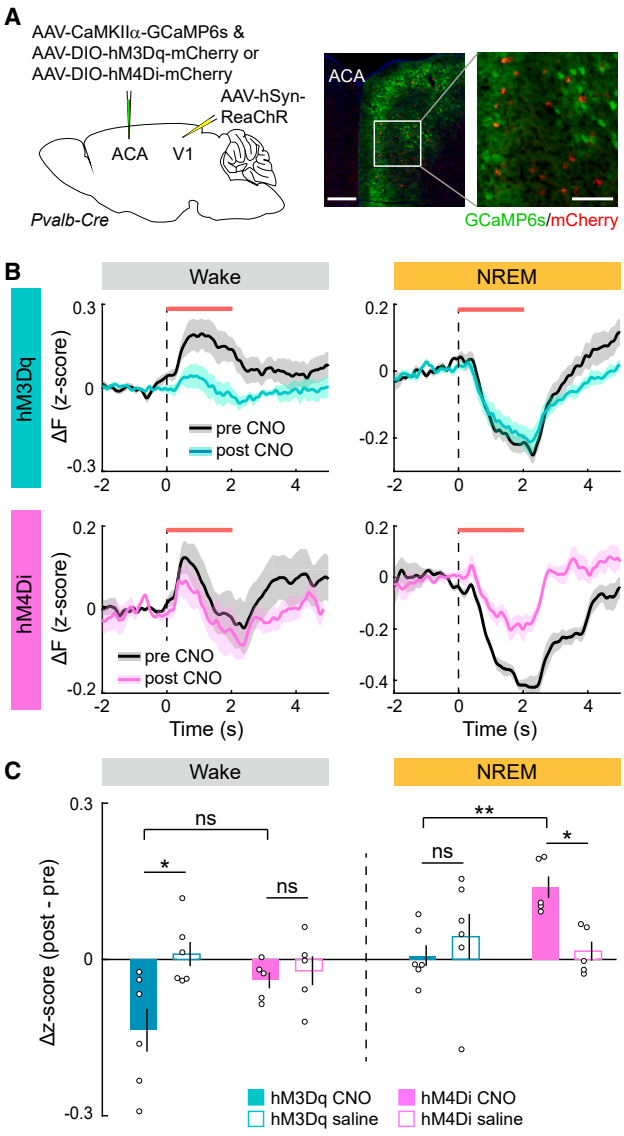

Figure 6. Effects of chemogenetic manipulation of ACA PV neurons on V1-evoked pyramidal neuron responses

(A) (Left) Schematic of chemogenetic manipulation of ACA PV neurons and calcium imaging of ACA pyramidal neuron activity. (Right) Expression of GCaMP6s (green) in pyramidal neurons and mCherry in PV neurons (red) in the ACA. Scale bars, 200 μm. The region in white box is enlarged. Scale bars, 100 μm.

(B) V1-evoked ACA pyramidal neuron activity before (black) and after (colored) CNO injection, during wakefulness (left) or NREM sleep (right), averaged across mice expressing hM3Dq (top) or hM4Di (bottom) in PV neurons. Baseline signal was subtracted for each trial before averaging. Horizontal red bar, laser stimulation.

(C) Summary of amplitude difference before and after CNO (filled) or saline (unfilled) injection. Each point represents one mouse. Wake: hM3Dq CNO vs. hM4Di CNO, $p = 0.1$; NREM: hM3Dq CNO vs. hM4Di CNO, $p = 0.0026$ (two-tailed unpaired t test).

Bar and error bar, mean ± SEM. Shading, ±SEM. *$p < 0.05$; **$p < 0.01$; ***$p < 0.001$; ns, not significant.

See also Figure S6.

(Figure 1I) but calcium signals changed the polarity (Figures 2F and S2I–S2K). This is likely because, whereas the calcium signals reflect pyramidal neuron activity, CBV is affected by the activity of excitatory and inhibitory neurons as well as non-neuronal cells (e.g., astrocytes).[44] Furthermore, calcium and fUSi measure cortical responses at different timescales. Although the inhibition of pyramidal neurons (lasting for 3–4 s) can be clearly detected in calcium imaging, it may be harder to detect in CBV signals that integrate brain activity over multiple seconds.

Chemogenetic activation and inactivation of basal forebrain cholinergic neurons strongly increased and decreased V1-evoked ACA responses, respectively (Figures 3 and 4), indicating that in addition to improving sensory processing in V1,[35,45] the cholinergic system also facilitates activity propagation from the visual cortex to the frontal cortex. Besides wakefulness, basal forebrain cholinergic neurons are also highly active during REM sleep,[13,14] which may explain the strong V1-evoked ACA activation during REM sleep (Figures S2A and S2B).

Calcium imaging from VIP, SST, NDNF, and PV interneurons showed different brain-state dependence of their activity (Figures 5A, 5C, 5E, and 5G). VIP, SST, and NDNF neurons are all more active during wakefulness than NREM sleep, consistent with their excitatory responses to cholinergic activation.[33–36,46] PV neurons, on the other hand, are inhibited by SST, VIP,[47] and layer 1 NDNF interneurons.[17,37] In addition, PV neurons receive long-range excitatory inputs from the claustrum,[48] which is more active during NREM sleep than wakefulness.[49,50] These inhibitory and excitatory inputs may all contribute to the higher activity of PV neurons during NREM sleep. Thus, at the transition from wakefulness to NREM sleep, the sources of GABAergic inputs to pyramidal neurons shift significantly from dendrite-targeting SST, VIP, and layer 1 NDNF neurons to perisomatic PV neurons. Somatic inhibition is particularly effective in suppressing the spiking output of pyramidal neurons.[51] The increased perisomatic inhibition during NREM sleep may effectively quench the V1-evoked excitation of ACA pyramidal neurons and thus prevent activity amplification through recurrent excitation that underlies cortical ignition.

We note that even during NREM sleep, PV neurons were activated only transiently by V1 stimulation (Figure 5H). The initial excitation is likely caused by the direct input from V1 pyramidal neurons.[22] The subsequent decrease in activity is counterintuitive, and it is likely to exemplify the "paradoxical effect" in an "inhibition-stabilized network."[52–55] An inhibition-stabilized network is a network in which recurrent connections among excitatory neurons are strong enough to destabilize the network, but feedback inhibition maintains its stability.[55] In such a network, an excitatory input to inhibitory (e.g., PV) neurons can cause a decrease in their activity together with a suppression of excitatory neuron activity, which is referred to as the paradoxical effect.[52–55] This is because the excitatory input (e.g., from V1) first increases spiking of the PV neurons, which inhibits nearby pyramidal neurons. However, the resulting decrease of pyramidal neuron activity reduces the excitation of PV neurons, leading to a decrease in PV neuron activity soon after the initial excitation (the paradoxical effect, due to strong local excitatory connections from pyramidal neurons to PV neurons). The net result is that the network settles to a steady state in which

both pyramidal and PV neurons exhibit reduced activity,[52–55] reminiscent of the V1-evoked ACA responses during NREM sleep (Figures 2F and 5H).

In summary, we found that cortical ignition is strongly suppressed during NREM sleep, a daily recurring brain state with diminished conscious awareness. Combining brain-wide fUSi with cell-type-specific calcium imaging and chemogenetic manipulation in mice, our study demonstrates a crucial role of cholinergic neuromodulation, which can act on multiple cortical neuron subtypes to control the gating of cortical ignition.

Limitations of the study

Although this study is directly motivated by the global neuronal workspace theory, the experiments were not designed to test the link between cortical ignition and conscious perception, which has been shown in humans and non-human primates.[2,3] Instead, the focus of this study is to understand the circuit mechanism underlying sleep/wake-dependent changes in cortical ignition at the level of genetically defined cell types. Due to the rarity of REM sleep in mice and the small number of laser trials in this state, we mainly focused on the comparison between NREM sleep and wakefulness. Previous studies have shown that sensory stimuli evoke different responses during REM and NREM sleep.[56,57] which could be related to changed cortical ignition (Figures S2A and S2B). In future studies, it would be of great interest to characterize cortico-cortical and cortico-subcortical activity propagation during REM sleep. Although we have demonstrated a critical role of basal forebrain cholinergic neurons in facilitating frontal cortical ignition, other neuromodulators such as noradrenaline, dopamine, serotonin, and histamine also promote brain arousal. How these neuromodulatory systems regulate cortical ignition remains to be investigated. Furthermore, although we have characterized spontaneous and V1-evoked activity of four major types of cortical interneurons across sleep-wake states, each type contains multiple subtypes with heterogeneous connectivity and function.[58] Their roles in regulating cortical ignition warrant further studies.

STAR★METHODS

Detailed methods are provided in the online version of this paper and include the following:

- KEY RESOURCES TABLE
- RESOURCE AVAILABILITY
  - Lead contact
  - Materials availability
  - Data and code availability
- EXPERIMENTAL MODEL AND STUDY PARTICIPANT DETAILS
- METHOD DETAILS
  - Virus preparation
  - Surgical procedures
  - Sleep-wake recording and analysis
  - Protocol of fUSi
  - Fiber photometry imaging
  - Two-photon imaging
  - Chemogenetic manipulation
  - Eye and whisker movement, movement speed and data analysis
  - fUSi data processing and analysis
  - Fiber photometry data analysis
  - Two-photon imaging data analysis
  - Immunohistochemistry and fluorescence *in situ* hybridization (FISH)
- QUANTIFICATION AND STATISTICAL ANALYSIS

SUPPLEMENTAL INFORMATION

Supplemental information can be found online at https://doi.org/10.1016/j.cell.2023.11.012.

ACKNOWLEDGMENTS

We thank C.F. Tso and L. Bui for help with the virus preparation and J. Zhang for helping to plot the figures. This work was supported by the Howard Hughes Medical Institute and Pivotal Life Sciences Chancellor's Chair in Neuroscience.

AUTHOR CONTRIBUTIONS

B.L. and Y.D. conceived and designed the study and wrote the paper with input from all other authors. B.L. and C.M. performed most of the experiments. B.L. wrote programs for data analysis. B.L., C.M., and X.D. analyzed the data. Y.-A.H., G.M., and A.U. provided software for ultrasound imaging and data analysis. D.S. and D.D. helped with the fiber photometry experiments. C.C. and L.L. helped with behavior monitoring. S.L. helped with histology. A.U. provided critical consultation and feedback. Y.D. supervised all aspects of the work.

DECLARATION OF INTERESTS

A.U. is the founder and a shareholder of AUTC OÜ Private Limited Company. Y.D. is a member of the advisory board of *Cell*.

Received: January 31, 2023
Revised: September 6, 2023
Accepted: November 9, 2023
Published: December 8, 2023

REFERENCES

1. Baars, B.J. (2005). Global workspace theory of consciousness: toward a cognitive neuroscience of human experience. Prog. Brain Res. *150*, 45–53.
2. van Vugt, B., Dagnino, B., Vartak, D., Safaai, H., Panzeri, S., Dehaene, S., and Roelfsema, P.R. (2018). The threshold for conscious report: signal loss and response bias in visual and frontal cortex. Science *360*, 537–542.
3. Mashour, G.A., Roelfsema, P., Changeux, J.P., and Dehaene, S. (2020). Conscious processing and the global neuronal workspace hypothesis. Neuron *105*, 776–798.
4. Strauss, M., Sitt, J.D., King, J.R., Elbaz, M., Azizi, L., Buiatti, M., Naccache, L., van Wassenhove, V., and Dehaene, S. (2015). Disruption of hierarchical predictive coding during sleep. Proc. Natl. Acad. Sci. USA *112*, E1353–E1362.
5. Yüzgeç, Ö., Prsa, M., Zimmermann, R., and Huber, D. (2018). Pupil size coupling to cortical states protects the stability of deep sleep via parasympathetic modulation. Curr. Biol. *28*, 392–400.e3.
6. Steriade, M., McCormick, D.A., and Sejnowski, T.J. (1993). Thalamocortical oscillations in the sleeping and aroused brain. Science *262*, 679–685.

7. Massimini, M., Ferrarelli, F., Huber, R., Esser, S.K., Singh, H., and Tononi, G. (2005). Breakdown of cortical effective connectivity during sleep. Science *309*, 2228–2232.
8. Hayat, H., Marmelshtein, A., Krom, A.J., Sela, Y., Tankus, A., Strauss, I., Fahoum, F., Fried, I., and Nir, Y. (2022). Reduced neural feedback signaling despite robust neuron and gamma auditory responses during human sleep. Nat. Neurosci. *25*, 935–943.
9. Sela, Y., Krom, A.J., Bergman, L., Regev, N., and Nir, Y. (2020). Sleep differentially affects early and late neuronal responses to sounds in auditory and perirhinal cortices. J. Neurosci. *40*, 2895–2905.
10. Brunner, C., Grillet, M., Sans-Dublanc, A., Farrow, K., Lambert, T., Macé, E., Montaldo, G., and Urban, A. (2020). A platform for brain-wide volumetric functional ultrasound imaging and analysis of circuit dynamics in awake mice. Neuron *108*, 861–875.e7.
11. Macé, É., Montaldo, G., Trenholm, S., Cowan, C., Brignall, A., Urban, A., and Roska, B. (2018). Whole-brain functional ultrasound imaging reveals brain modules for visuomotor integration. Neuron *100*, 1241–1251.e7.
12. Sans-Dublanc, A., Chrzanowska, A., Reinhard, K., Lemmon, D., Nuttin, B., Lambert, T., Montaldo, G., Urban, A., and Farrow, K. (2021). Optogenetic fUSI for brain-wide mapping of neural activity mediating collicular-dependent behaviors. Neuron *109*, 1888–1905.e10.
13. Lee, M.G., Hassani, O.K., Alonso, A., and Jones, B.E. (2005). Cholinergic basal forebrain neurons burst with theta during waking and paradoxical sleep. J. Neurosci. *25*, 4365–4369.
14. Xu, M., Chung, S., Zhang, S., Zhong, P., Ma, C., Chang, W.C., Weissbourd, B., Sakai, N., Luo, L., Nishino, S., et al. (2015). Basal forebrain circuit for sleep-wake control. Nat. Neurosci. *18*, 1641–1647.
15. Rudy, B., Fishell, G., Lee, S., and Hjerling-Leffler, J. (2011). Three groups of interneurons account for nearly 100% of neocortical GABAergic neurons. Dev. Neurobiol. *71*, 45–61.
16. Zhou, X., Rickmann, M., Hafner, G., and Staiger, J.F. (2017). Subcellular targeting of VIP boutons in mouse barrel cortex is layer-dependent and not restricted to interneurons. Cereb. Cortex *27*, 5353–5368.
17. Anastasiades, P.G., and Carter, A.G. (2021). Circuit organization of the rodent medial prefrontal cortex. Trends Neurosci. *44*, 550–563.
18. Cohen-Kashi Malina, K., Tsivourakis, E., Kushinsky, D., Apelblat, D., Shtiglitz, S., Zohar, E., Sokoletsky, M., Tasaka, G.I., Mizrahi, A., Lampl, I., et al. (2021). NDNF interneurons in layer 1 gain-modulate whole cortical columns according to an animal's behavioral state. Neuron *109*, 2150–2164.e5.
19. Lin, J.Y., Knutsen, P.M., Muller, A., Kleinfeld, D., and Tsien, R.Y. (2013). ReaChR: a red-shifted variant of channelrhodopsin enables deep transcranial optogenetic excitation. Nat. Neurosci. *16*, 1499–1508.
20. Lee, J.H., Durand, R., Gradinaru, V., Zhang, F., Goshen, I., Kim, D.S., Fenno, L.E., Ramakrishnan, C., and Deisseroth, K. (2010). Global and local fMRI signals driven by neurons defined optogenetically by type and wiring. Nature *465*, 788–792.
21. Montaldo, G., Urban, A., and Macé, E. (2022). Functional ultrasound neuroimaging. Annu. Rev. Neurosci. *45*, 491–513.
22. Zhang, S., Xu, M., Chang, W.C., Ma, C., Hoang Do, J.P., Jeong, D., Lei, T., Fan, J.L., and Dan, Y. (2016). Organization of long-range inputs and outputs of frontal cortex for top-down control. Nat. Neurosci. *19*, 1733–1742.
23. Bergel, A., Deffieux, T., Demené, C., Tanter, M., and Cohen, I. (2018). Local hippocampal fast gamma rhythms precede brain-wide hyperemic patterns during spontaneous rodent REM sleep. Nat. Commun. *9*, 5364.
24. Fisch, L., Privman, E., Ramot, M., Harel, M., Nir, Y., Kipervasser, S., Andelman, F., Neufeld, M.Y., Kramer, U., Fried, I., et al. (2009). Neural "ignition": enhanced activation linked to perceptual awareness in human ventral stream visual cortex. Neuron *64*, 562–574.
25. Perry, E., Walker, M., Grace, J., and Perry, R. (1999). Acetylcholine in mind: a neurotransmitter correlate of consciousness? Trends Neurosci. *22*, 273–280.
26. Do, J.P., Xu, M., Lee, S.H., Chang, W.C., Zhang, S., Chung, S., Yung, T.J., Fan, J.L., Miyamichi, K., Luo, L., et al. (2016). Cell type-specific long-range connections of basal forebrain circuit. eLife *5*, e13214.
27. Pal, D., Dean, J.G., Liu, T., Li, D., Watson, C.J., Hudetz, A.G., and Mashour, G.A. (2018). Differential role of prefrontal and parietal cortices in controlling level of consciousness. Curr. Biol. *28*, 2145–2152.e5.
28. Aston-Jones, G., and Bloom, F.E. (1981). Activity of norepinephrine-containing locus coeruleus neurons in behaving rats anticipates fluctuations in the sleep-waking cycle. J. Neurosci. *1*, 876–886.
29. Sternson, S.M., and Roth, B.L. (2014). Chemogenetic tools to interrogate brain functions. Annu. Rev. Neurosci. *37*, 387–407.
30. Chen, L., Yin, D., Wang, T.X., Guo, W., Dong, H., Xu, Q., Luo, Y.J., Cherasse, Y., Lazarus, M., Qiu, Z.L., et al. (2016). Basal forebrain cholinergic neurons primarily contribute to inhibition of electroencephalogram delta activity, rather than inducing behavioral wakefulness in mice. Neuropsychopharmacology *41*, 2133–2146.
31. Esser, S.K., Hill, S., and Tononi, G. (2009). Breakdown of effective connectivity during slow wave sleep: investigating the mechanism underlying a cortical gate using large-scale modeling. J. Neurophysiol. *102*, 2096–2111.
32. Joglekar, M.R., Mejias, J.F., Yang, G.R., and Wang, X.J. (2018). Inter-areal balanced amplification enhances signal propagation in a large-scale circuit model of the primate cortex. Neuron *98*, 222–234.e8.
33. Chen, N., Sugihara, H., and Sur, M. (2015). An acetylcholine-activated microcircuit drives temporal dynamics of cortical activity. Nat. Neurosci. *18*, 892–902.
34. Alitto, H.J., and Dan, Y. (2012). Cell-type-specific modulation of neocortical activity by basal forebrain input. Front. Syst. Neurosci. *6*, 79.
35. Fu, Y., Tucciarone, J.M., Espinosa, J.S., Sheng, N., Darcy, D.P., Nicoll, R.A., Huang, Z.J., and Stryker, M.P. (2014). A cortical circuit for gain control by behavioral state. Cell *156*, 1139–1152.
36. Gasselin, C., Hohl, B., Vernet, A., Crochet, S., and Petersen, C.C.H. (2021). Cell-type-specific nicotinic input disinhibits mouse barrel cortex during active sensing. Neuron *109*, 778–787.e3.
37. Letzkus, J.J., Wolff, S.B., Meyer, E.M., Tovote, P., Courtin, J., Herry, C., and Lüthi, A. (2011). A disinhibitory microcircuit for associative fear learning in the auditory cortex. Nature *480*, 331–335.
38. Sun, Q., Li, X., Li, A., Zhang, J., Ding, Z., Gong, H., and Luo, Q. (2020). Ventral hippocampal-prefrontal interaction affects social behavior via parvalbumin positive neurons in the medial prefrontal cortex. iScience *23*, 100894.
39. Cummings, K.A., and Clem, R.L. (2020). Prefrontal somatostatin interneurons encode fear memory. Nat. Neurosci. *23*, 61–74.
40. Xu, H., Liu, L., Tian, Y., Wang, J., Li, J., Zheng, J., Zhao, H., He, M., Xu, T.L., Duan, S., et al. (2019). A disinhibitory microcircuit mediates conditioned social fear in the prefrontal cortex. Neuron *102*, 668–682.e5.
41. Lee, A.T., Cunniff, M.M., See, J.Z., Wilke, S.A., Luongo, F.J., Ellwood, I.T., Ponnavolu, S., and Sohal, V.S. (2019). VIP interneurons contribute to avoidance behavior by regulating information flow across hippocampal-prefrontal networks. Neuron *102*, 1223–1234.e4.
42. Brécier, A., Borel, M., Urbain, N., and Gentet, L.J. (2022). Vigilance and behavioral state-dependent modulation of cortical neuronal activity throughout the sleep/wake cycle. J. Neurosci. *42*, 4852–4866.
43. Niethard, N., Brodt, S., and Born, J. (2021). Cell-type-specific dynamics of calcium activity in cortical circuits over the course of slow-wave sleep and rapid eye movement sleep. J. Neurosci. *41*, 4212–4222.
44. Winder, A.T., Echagarruga, C., Zhang, Q.G., and Drew, P.J. (2017). Weak correlations between hemodynamic signals and ongoing neural activity during the resting state. Nat. Neurosci. *20*, 1761–1769.
45. Pinto, L., Goard, M.J., Estandian, D., Xu, M., Kwan, A.C., Lee, S.H., Harrison, T.C., Feng, G., and Dan, Y. (2013). Fast modulation of visual perception by basal forebrain cholinergic neurons. Nat. Neurosci. *16*, 1857–1863.

46. Poorthuis, R.B., Muhammad, K., Wang, M., Verhoog, M.B., Junek, S., Wrana, A., Mansvelder, H.D., and Letzkus, J.J. (2018). Rapid neuromodulation of layer 1 interneurons in human neocortex. Cell Rep. *23*, 951–958.

47. Pfeffer, C.K., Xue, M., He, M., Huang, Z.J., and Scanziani, M. (2013). Inhibition of inhibition in visual cortex: the logic of connections between molecularly distinct interneurons. Nat. Neurosci. *16*, 1068–1076.

48. Jackson, J., Karnani, M.M., Zemelman, B.V., Burdakov, D., and Lee, A.K. (2018). Inhibitory control of prefrontal cortex by the claustrum. Neuron *99*, 1029–1039.e4.

49. Norimoto, H., Fenk, L.A., Li, H.H., Tosches, M.A., Gallego-Flores, T., Hain, D., Reiter, S., Kobayashi, R., Macias, A., Arends, A., et al. (2020). A claustrum in reptiles and its role in slow-wave sleep. Nature *578*, 413–418.

50. Narikiyo, K., Mizuguchi, R., Ajima, A., Shiozaki, M., Hamanaka, H., Johansen, J.P., Mori, K., and Yoshihara, Y. (2020). The claustrum coordinates cortical slow-wave activity. Nat. Neurosci. *23*, 741–753.

51. Miles, R., Tóth, K., Gulyás, A.I., Hájos, N., and Freund, T.F. (1996). Differences between somatic and dendritic inhibition in the hippocampus. Neuron *16*, 815–823.

52. Romero-Sosa, J.L., Motanis, H., and Buonomano, D.V. (2021). Differential excitability of PV and SST neurons results in distinct functional roles in inhibition stabilization of UP states. J. Neurosci. *41*, 7182–7196.

53. Sanzeni, A., Akitake, B., Goldbach, H.C., Leedy, C.E., Brunel, N., and Histed, M.H. (2020). Inhibition stabilization is a widespread property of cortical networks. eLife *9*, e54875.

54. Ozeki, H., Finn, I.M., Schaffer, E.S., Miller, K.D., and Ferster, D. (2009). Inhibitory stabilization of the cortical network underlies visual surround suppression. Neuron *62*, 578–592.

55. Tsodyks, M.V., Skaggs, W.E., Sejnowski, T.J., and McNaughton, B.L. (1997). Paradoxical effects of external modulation of inhibitory interneurons. J. Neurosci. *17*, 4382–4388.

56. Tseng, Y.T., Zhao, B., Chen, S., Ye, J., Liu, J., Liang, L., Ding, H., Schaefke, B., Yang, Q., Wang, L., et al. (2022). The subthalamic corticotropin-releasing hormone neurons mediate adaptive REM-sleep responses to threat. Neuron *110*, 1223–1239.e8.

57. Hayat, H., Regev, N., Matosevich, N., Sales, A., Paredes-Rodriguez, E., Krom, A.J., Bergman, L., Li, Y., Lavigne, M., Kremer, E.J., et al. (2020). Locus coeruleus norepinephrine activity mediates sensory-evoked awakenings from sleep. Sci. Adv. *6*, eaaz4232.

58. Yuste, R., Hawrylycz, M., Aalling, N., Aguilar-Valles, A., Arendt, D., Armañanzas, R., Ascoli, G.A., Bielza, C., Bokharaie, V., Bergmann, T.B., et al. (2020). A community-based transcriptomics classification and nomenclature of neocortical cell types. Nat. Neurosci. *23*, 1456–1468.

59. Chen, T.W., Wardill, T.J., Sun, Y., Pulver, S.R., Renninger, S.L., Baohan, A., Schreiter, E.R., Kerr, R.A., Orger, M.B., Jayaraman, V., et al. (2013). Ultrasensitive fluorescent proteins for imaging neuronal activity. Nature *499*, 295–300.

60. Krashes, M.J., Koda, S., Ye, C., Rogan, S.C., Adams, A.C., Cusher, D.S., Maratos-Flier, E., Roth, B.L., and Lowell, B.B. (2011). Rapid, reversible activation of AgRP neurons drives feeding behavior in mice. J. Clin. Invest. *121*, 1424–1428.

61. Hauswirth, W.W., Lewin, A.S., Zolotukhin, S., and Muzyczka, N. (2000). Production and purification of recombinant adeno-associated virus. Methods Enzymol. *316*, 743–761.

62. Liu, D., Li, W., Ma, C., Zheng, W., Yao, Y., Tso, C.F., Zhong, P., Chen, X., Song, J.H., Choi, W., et al. (2020). A common hub for sleep and motor control in the substantia nigra. Science *367*, 440–445.

63. Rungta, R.L., Osmanski, B.F., Boido, D., Tanter, M., and Charpak, S. (2017). Light controls cerebral blood flow in naive animals. Nat. Commun. *8*, 14191.

64. Horio, N., and Liberles, S.D. (2021). Hunger enhances food-odour attraction through a neuropeptide Y spotlight. Nature *592*, 262–266.

65. Li, Y., Lu, H., Cheng, P.L., Ge, S., Xu, H., Shi, S.H., and Dan, Y. (2012). Clonally related visual cortical neurons show similar stimulus feature selectivity. Nature *486*, 118–121.

66. Ahmadlou, M., Houba, J.H.W., van Vierbergen, J.F.M., Giannouli, M., Gimenez, G.A., van Weeghel, C., Darbanfouladi, M., Shirazi, M.Y., Dziubek, J., Kacem, M., et al. (2021). A cell type-specific cortico-subcortical brain circuit for investigatory and novelty-seeking behavior. Science *372*, eabe9681.

67. Mathis, A., Mamidanna, P., Cury, K.M., Abe, T., Murthy, V.N., Mathis, M.W., and Bethge, M. (2018). DeepLabCut: markerless pose estimation of user-defined body parts with deep learning. Nat. Neurosci. *21*, 1281–1289.

68. Segalin, C., Williams, J., Karigo, T., Hui, M., Zelikowsky, M., Sun, J.J., Perona, P., Anderson, D.J., and Kennedy, A. (2021). The Mouse Action Recognition System (MARS) software pipeline for automated analysis of social behaviors in mice. eLife *10*.

69. Todorov, M.I., Paetzold, J.C., Schoppe, O., Tetteh, G., Shit, S., Efremov, V., Todorov-Völgyi, K., Düring, M., Dichgans, M., Piraud, M., et al. (2020). Machine learning analysis of whole mouse brain vasculature. Nat. Methods *17*, 442–449.

70. Lerner, T.N., Shilyansky, C., Davidson, T.J., Evans, K.E., Beier, K.T., Zalocusky, K.A., Crow, A.K., Malenka, R.C., Luo, L., Tomer, R., et al. (2015). Intact-brain analyses reveal distinct information carried by SNc dopamine subcircuits. Cell *162*, 635–647.

71. Li, B., Nguyen, T.P., Ma, C., and Dan, Y. (2020). Inhibition of impulsive action by projection-defined prefrontal pyramidal neurons. Proc. Natl. Acad. Sci. USA *117*, 17278–17287.

72. Otis, J.M., Namboodiri, V.M., Matan, A.M., Voets, E.S., Mohorn, E.P., Kosyk, O., McHenry, J.A., Robinson, J.E., Resendez, S.L., Rossi, M.A., et al. (2017). Prefrontal cortex output circuits guide reward seeking through divergent cue encoding. Nature *543*, 103–107.

73. Ahrens, M.B., Li, J.M., Orger, M.B., Robson, D.N., Schier, A.F., Engert, F., and Portugues, R. (2012). Brain-wide neuronal dynamics during motor adaptation in zebrafish. Nature *485*, 471–477.

74. Harvey, C.D., Coen, P., and Tank, D.W. (2012). Choice-specific sequences in parietal cortex during a virtual-navigation decision task. Nature *484*, 62–68.

75. Pho, G.N., Goard, M.J., Woodson, J., Crawford, B., and Sur, M. (2018). Task-dependent representations of stimulus and choice in mouse parietal cortex. Nat. Commun. *9*, 2596.

STAR★METHODS

KEY RESOURCES TABLE

REAGENT or RESOURCE	SOURCE	IDENTIFIER
Antibodies		
eGFP antibody	Aves Labs	Cat# GFP-1020; RRID: AB_10000240
Bacterial and virus strains		
AAV9-CAG-Flex-GCaMP6s	Chen et al.[59]	Addgene # 100842-AAV9
AAV2-hSyn-DIO-hM3D(Gq)-mCherry	Krashes et al.[60]	Addgene # 44361-AAV2
AAV2-hSyn-DIO-hM4D(Gi)-mCherry	Krashes et al.[60]	Addgene # 44362-AAV2
AAV2-hSyn-DIO-EGFP	Bryan Roth's Lab	Addgene # 50457-AAV2
AAV9-CaMKIIα-GCaMP6s	James M. Wilson's Lab	Addgene # 107790-AAV9
AAV2-hSyn-ReaChR-mCitrine	Lin et al.[19]	Addgene plasmid # 50954
AAV2-hSyn-Flex-ReaChR-mCitrine	Lin et al.[19]	Addgene plasmid # 50955
Chemicals, peptides, and recombinant proteins		
Clozapine-N-oxide	Sigma-Aldrich	Cat# C0832
Experimental models: Organisms/strains		
Mouse: C57BL/6J	The Jackson Laboratory	Cat# 000664; RRID:IMSR_JAX:000664
Mouse: Chat-Cre	The Jackson Laboratory	Cat# 006410; RRID:IMSR_JAX:006410
Mouse: Camk2α-Cre	The Jackson Laboratory	Cat# 005359; RRID:IMSR_JAX:005359
Mouse: Vip-Cre	The Jackson Laboratory	Cat# 010908; RRID:IMSR_JAX:010908
Mouse: Sst-Cre	The Jackson Laboratory	Cat# 013044; RRID:IMSR_JAX:013044
Mouse: Ndnf-Cre	The Jackson Laboratory	Cat# 030757; RRID:IMSR_JAX:030757
Mouse: Pvalb-Cre	The Jackson Laboratory	Cat# 017320; RRID:IMSR_JAX:017320
Oligonucleotides		
Slc32a1 In situ hybridization probe	Advanced Cell Diagnostics	Cat# 319191
Slc17a7 In situ hybridization probe	Advanced Cell Diagnostics	Cat# 501101
Pvalb In situ hybridization probe	Advanced Cell Diagnostics	Cat# 421931
Software and algorithms		
MATLAB	Mathworks	https://www.mathworks.com/products/matlab.html
Prism	GraphPad	Version 9.2.0
Synapse	Tucker-Davis Technologies	N/A
OpenEx	Tucker-Davis Technologies	N/A
ImageJ	NIH	https://imagej.nih.gov/ij/
Code for fUSi data registration and segmentation	Brunner et al.[10]	supplemental information at https://www.sciencedirect.com/science/article/pii/S0896627320307200#app2
Other		
Ultrasound scanner Vantage 128	Verasonics	https://verasonics.com/vantage-systems/
High-frequency ultrasound probe L22v14	Verasonics	https://verasonics.com/high-frequency-transducers/
Real-time fUSi data processing and display	AUTC	https://fusi-functional-ultrasound-imaging.com
Microprecision motor	Zaber	X-LRM-DE
Silicone rubber	Smooth-on	Body Double-Fast Set
Mating sleeve	Thorlabs	ADAF1
Optical fibers_200 mm diameter	Neurophotometrics	N/A
PZ5 amplifier	Tucker-Davis Technologies	https://www.tdt.com/component/pz5-neurodigitizer-amplifier/
TDT RZ10x real-time processor	Tucker-Davis Technologies	https://www.tdt.com/docs/hardware/rz10-lux-integrated-processor/
635 nm collimated diode laser	Laserglow	D631001FL
Minicube-wavelength division	Doric Lenses	N/A

RESOURCE AVAILABILITY

Lead contact

Further information and requests for resources and reagents should be directed to and will be fulfilled by the lead contact, Yang Dan (ydan@berkeley.edu).

Materials availability

This study did not generate new unique reagents.

Data and code availability

- All data necessary to understand and assess the conclusions of this manuscript are presented in the paper and the supplemental information.
- The code for fUSi data registration and segmentation is described in the key resources table. Custom data analysis code has been provided in supplemental information.
- Any additional information required to reanalyze the data reported in this paper is available from the lead contact upon request.

EXPERIMENTAL MODEL AND STUDY PARTICIPANT DETAILS

All procedures were approved by Animal Care and Use Committees of the University of California, Berkeley. C57BL/6J (000664), *Chat-Cre* (006410), *Camk2α-Cre* (005359), *Vip-Cre* (010908), *Sst-Cre* (013044), *Ndnf-Cre* (030757), *Pvalb-Cre* (017320) and *Vglut1-Cre* (037512) mice were obtained from The Jackson Laboratory. Mice of specific genotypes were randomly assigned to experimental and control groups. Experimental and control animals were subjected to exactly the same surgical and behavioral manipulations. Investigators were not blinded to animal identity and outcome assessment. All the experiments were performed on adult animals (2−6 months) of both genders. Statistical comparisons did not detect any significant differences between male and female mice, so the data were combined to complete final group sizes. Mice were housed in 12 h light−dark cycles (lights on at 07:00 and off at 19:00) with free access to food and water. Animals with implants were housed individually.

METHOD DETAILS

Virus preparation

AAV2-hSyn-DIO-hM3D(Gq)-mCherry (Addgene 44361-AAV2), AAV2-hSyn-DIO-hM4D(Gi)-mCherry (Addgene 44362-AAV2), AAV2-hSyn-DIO-EGFP (Addgene, 50457-AAV2), AAV9-CAG-Flex-GCaMP6s (Addgene 100842-AAV9) and AAV9-CaMKIIα-GCaMP6s (Addgene 107790-AAV9) were obtained from the Addgene. AAV2-hSyn-ReaChR-mCitrine (Addgene, plasmid 50954) and AAV2-hSyn-Flex-ReaChR-mCitrine (Addgene, plasmid 50955) were prepared in house according to previously described protocols.[61] The final titer of all the viruses was estimated to be $\geq 1 \times 10^{13}$ gc/ml.

Surgical procedures

For all the surgeries, mice were anesthetized with 1.5%−2% isoflurane and placed on a stereotaxic frame. Heating pad was used to keep the body temperature stable during the whole procedure. Eye ointment was applied to keep the eyes from drying. After shaving hairs and asepsis with Betadine and medical alcohol, an incision was made to the skin to expose the skull.

For experiments with virus injection, a craniotomy (0.5−1 mm diameter) was made on top of the target region (see below for coordinates), and 0.1−0.3 μl virus was injected into the target region using Nanoject II (Drummond Scientific) via a micro pipette. For chemogenetic activation/inactivation of the basal forebrain cholinergic neurons or local chemogenetic modulation of cholinergic input to the ACA, AAV2-hSyn-DIO-hM3D(Gq)-mCherry or AAV2-hSyn-DIO-hM4D(Gi)-mCherry was bilaterally injected into the basal forebrain. For chemogenetic manipulation of ACA PV neurons and NDNF neurons, AAV2-hSyn-DIO-hM3D(Gq)-mCherry or AAV2-hSyn-DIO-hM4D(Gi)-mCherry mixed with AAV9-CamKIIα-GCaMP6s (ratio, 4:1) were unilaterally injected into the ACA.

For sleep-wake recording, EEG and EMG recording electrodes were implanted. EEG recordings were made from two stainless steel screws on top of the cortex, at anteroposterior (AP) –3 mm, mediolateral (ML) 2.5 mm (parietal cortex) and AP +1.5 mm, ML 1.5 mm (frontal cortex), respectively. Two EMG electrodes were inserted into the neck musculature. A reference screw was inserted into the skull on top of the left cerebellum. Insulated leads from the EEG and EMG electrodes were soldered to a pin header, which was secured to the skull using dental cement.

For experiments with ultrasound imaging, a stainless steel headplate was firmly attached to the skull and dental cement was applied generally to cover the rim of the headplate. A large cranial window (AP: +2 to –4.5 mm, ML +3.5 to –3.5 mm) was made with a drill.[10,11] Dura was kept intact. For optogenetic V1 activation, a guide mating sleeve (Thorlabs, ADAF1) was chronically implanted close to V1 at a 30°–40° angle, to avoid physical interference with the ultrasound transducer (Verasonics, L22–14v). The

cranial window was covered with silicone rubber (Smooth-on, Body Double-Fast Set) for protection. For sleep-wake recording, a smaller cranial window (AP: +2 to –4.5 mm, ML +0.5 to –3.5 mm) was made. EEG and EMG recording electrodes were implanted in the opposite side of the skull to the cranial window as described above.

For experiments with fiber photometry imaging and optogenetic V1 activation, two craniotomies (0.5–1mm in diameter) were made on top of V1 and ACA, and optical fibers (Neurophotometrics, 200 μm core, 0.37 NA) with FC ferrule were implanted into V1 (layers 2-4) and ACA (layers 2/3 and upper layer 5), separately. For experiments with local chemogenetic modulation of cholinergic input, a cannula (Plastics One Technologies) was implanted into the ACA for local infusion. Dental cement was applied to cover the exposed skull completely and to secure the implants for EEG and EMG recordings to the screws.

For experiments with two-photon imaging, a stainless steel headplate was firmly attached to the skull and dental cement was applied to cover the rim of the headplate. A craniotomy (3 x 3 mm in diameter) was made on top of the ACA. Dura was kept intact. The craniotomy was centered at ~0.5 mm AP and ~0.5 mm ML. A 4 x 4-mm glass coverslip (Warner Instruments) was cut with a diamond-point pen and attached to a 3 x 3-mm coverslip by UV glue (Norland, Norland Optical Adhesive). After being sterilized and dried, the combined coverslips were slowly lowered into the craniotomy. For optogenetic V1 activation, an optical fiber (Neurophotometrics, 200 μm core, 0.37 NA) with FC ferrule was implanted into the V1 at a 5°–10° angle, to avoid physical interference with the objective (Olympus, XLUMPlanFI, 0.95 NA) of the microscope (Sutter Instrument, Movable Objective Microscope). Dental cement was applied to cover the exposed skull completely and to secure the implants for EEG and EMG recordings to the screws.

After surgery, mice were allowed to recover from anesthesia on a heating pad before returned to their home cage. Buprenorphine (0.1 mg/kg) was given prior to surgery, and meloxicam (5–10 mg/kg) was given prior to surgery and once the following day. Anti-inflammatory drug (dexamethasone 0.2 mg/kg) was applied for 5 days after the cranial window surgery. All experiments were carried out at least one week after surgery.

Stereotaxic coordinates for virus injection and optic fiber implantation:
V1: AP -3.1 mm, ML 2.5 mm, DV 0.5 mm.
ACA: AP 0.5 mm, ML 0.3 mm, DV 0.7 mm.
Basal forebrain: AP 0.1 mm, ML 1.5 mm, DV 5.3 mm.

Sleep-wake recording and analysis

Experiments were carried out in sound-attenuating boxes between 10:00 am and 19:00 pm. EEG and EMG electrodes were connected to flexible recording cables via a mini-connector. Recordings started after 20–30 min of habituation. The signals were recorded with a Tucker-Davis Technologies (TDT) PZ5 amplifier, filtered (0–300 Hz) and digitized at 1,500 Hz. Spectral analysis was carried out using fast Fourier transform, and brain states were classified into wake, NREM and REM states (wake: desynchronized EEG and high EMG activity; NREM: synchronized EEG with high-amplitude, low-frequency (1–4 Hz) activity and low EMG activity; REM: high EEG power at theta frequencies (6–9 Hz) and low EMG activity). The classification was made with a 5 s bin using a custom-written graphical user interface (programmed in MATLAB, MathWorks). Brain states classified based on EEG signals recorded from the frontal and parietal cortical areas are virtually identical, so the EEG channel with a higher signal/noise ratio was used. Bootstrap[62] was used to analyze the effects of laser stimulation on brain states (Figure S1D).

Protocol of fUSi

The awake head-fixed mice were habituated under the ultrasound transducer every day for at least 6 days prior to experiments. Before imaging, the silicone rubber was removed and the cranial window was covered with a 2%–3% agarose layer to reduce brain movement. Acoustic gel (Aquasonic, Clear Ultrasound Transmission Gel, 1 ml) was applied on the cranial window for ultrasound coupling before placing the ultrasound transducer. A 635 nm collimated diode laser (Laserglow, D631001FL) was then connected to the guide mating sleeve using a ferrule patch cable (Thorlabs, M81L01). Therefore, agarose and acoustic gel filled the space between the cortex and the ferrule. For optogenetic V1 activation, a constant light (10–20 mW at ferrule tip) lasting for 2 s was used. The ultrasound transducer, connected to an ultrasound scanner (Verasonics, Vantage 128) controlled by a dedicated high-performance computing (HPC) workstation for real-time GP-GPU processing (fUSi HPC module, AUTC, Estonia), was lowered down to 3 mm from the brain. The transducer was moved along the lateral axis by a linear microprecision motor (Zaber). At the beginning of each imaging session, a reference anatomical scan was acquired for registration (61 sagittal planes from ML +3 mm to –3 mm, 100 μm steps). Next, a functional scan (1 Hz) was acquired (21 sagittal planes, 15 min imaging time per plane, from ML +3 mm to –3 mm, 300 μm steps). With the 1D ultrasound probe used in this study, CBV imaging was acquired at one sagittal plane per optogenetic stimulation trial. To minimize the impact of non-stationarity (e.g, adaptation of responses over repeated stimulation), the data at different sagittal planes were acquired at a random sequence. Light pulses were generated using the TDT system and inter-trial interval was set randomly from a uniform distribution between 60 and 100 s. The laser was also applied to V1 of control mice not expressing ReaChR (Figure S1A) to confirm that the observed responses in mice with ReaChR were not due to laser-evoked visual inputs from the eyes or heat generated by laser,[63] but originated from the activation through the red-shifted channelrhodopsin variant ReaChR. In a subset of mice, after the anatomical scan, we adjusted the position of the transducer to image simultaneously the visual cortex and other brain regions including the frontal cortex and some thalamic areas. Brain regions were identified based on anatomical landmarks matching those from the anatomical scan, which was registered to the Allen Mouse Brain Atlas (see "fUSi data processing and analysis" below).

To measure activity across natural sleep-wake cycles, mice were habituated to sleep under a head-fixed condition. The head of the mice was kept at a 30° angle to imitate the natural sleep position during head fixation.[5] Mice were kept head-fixed under the ultrasound transducer for ~15, ~30 and ~45 min for the first three days. The duration of head-fixation increased by 20 to 30 min per day, reaching a maximum of ~4 h. During imaging sessions, mice were allowed 10 min of habituation after being head-fixed before imaging started. EEG and EMG were recorded as described above.

Fiber photometry imaging

To record neuronal calcium activity in the ACA and V1, fiber photometry was performed using a TDT RZ10x real-time processor.[64] Mice were in their home cages placed in sound-attenuating boxes, and were attached via optical fibers (Neurophotometrics, 200 μm core, 0.37 NA) implanted in the ACA and V1 to a fluorescence minicube (Doric Lenses) during fiber photometry imaging. Fluorescence elicited by 405 nm (serves as an isosbestic wavelength for GCaMP6s) and 465 nm (calcium-dependent GCaMP6s fluorescence) LEDs was filtered through the Doric minicubes and collected with an integrated photosensor on the RZ10x. Signals were pre-processed using the TDT Synapse software and collected at a sampling frequency of 1018 Hz.

For experiments with ACA fiber photometry imaging and optogenetic V1 activation, an optical fiber implanted in the ACA was attached to a Doric minicube for fiber photometry imaging. Another optic fiber implanted in V1 was attached through an FC/PC adaptor to a 635 nm collimated diode laser (Laserglow, D631001FL). In a subset of the experiments with both ACA and V1 fiber photometry imaging and optogenetic V1 activation, the optic fiber implanted in V1 was coupled to a minicube-wavelength division (Doric Lenses), which combines the lights from a Doric minicube and a 635 nm laser. Laser pulses (constant light, 2–4 mW at fiber tip, 2 s) were generated using the TDT Synapse software, and inter-trial interval was set randomly from a uniform distribution between 60 and 100 s.

Two-photon imaging

Two-photon imaging was performed using a custom two-photon microscope that has been described previously.[65] Briefly, the microscope (Sutter Instrument, Movable Objective Microscope) was controlled by the ScanImage software and the objective was a 20× water immersion lens (Olympus, XLUMPlanFI, 0.95 NA). The InSight X3 laser (Spectra-Physics) was tuned to 920nm and ~40 mV output for GCaMP6s imaging (as measured under the objective). The intensity of excitation from the InSight X3 laser was controlled by a Pockels cell (Conoptics, 350-80-LA-02). Fluorescence emission was filtered (Semrock, FF01-535/50-25, FF01-525/39-25) and collected using a GaAsP PMT (Hamamatsu, H10770PA-40). Imaging was performed at a frame rate of 1.68 Hz and pixel resolution of 256 × 256. To measure activity across sleep-wake cycles, mice were habituated to sleep under a head-fixed condition. Mice were kept head-fixed under the two-photon system for ~15, ~30 and ~45 min for the first three days. The duration of head-fixation increased by 20 to 30 min per day, reaching a maximum of ~4 h. During imaging sessions, mice were allowed 10 min of habituation after being head-fixed before imaging started. The optic fiber implanted in V1 was attached through an FC/PC adaptor to a 635 nm collimated diode laser (Laserglow, D631001FL) for optogenetic V1 activation. EEG and EMG were recorded as described above.

Chemogenetic manipulation

Saline (0.9% NaCl) or clozapine N–oxide (CNO, Sigma, C0832, 1 mg/kg) was intraperitoneally injected into mice expressing hM4Di-mCherry in the basal forebrain or mice expressing hM3Dq-mCherry or hM4Di-mCherry in the ACA. To prevent excessive increase of wakefulness induced by activating basal forebrain cholinergic neurons,[14] CNO was diluted three times before injected into mice expressing hM3Dq-mCherry in the basal forebrain. For local chemogenetic modulation of cholinergic input, artificial cerebrospinal fluid (ACSF) or CNO (1 mM, 250 nl, dissolved in ACSF) was infused into the ACA through the cannula, at 50 nl/min using a microinfusion pump. In each session (functional ultrasound imaging or fiber photometry imaging), imaging was performed for 2 h baseline period before saline/ACSF or CNO injection/infusion and another 2 h afterwards. Each mouse was imaged for 4–6 sessions, and CNO was given randomly in half of the sessions and saline/ACSF in the other half (at the same circadian time on different days). Data were averaged across mice for statistical comparisons.

Eye and whisker movement, movement speed and data analysis

The eye and whiskers of the head-fixed mice were monitored using an infrared video camera with a sampling rate of 10 Hz. The coordinates of the center of the eye were extracted from each video frame, and the eye movement was quantified by tracking the change in Euclidean distance of the eye center over time. Whisker movement was determined by computing the absolute difference between the average intensity of the current frame and that of the previous frame.[66] Movement of freely moving mice was recorded using a video camera with a sampling rate of 20 Hz. Markerless pose estimation was performed with the DeepLabCut toolbox (version 2.2.3).[67] Seven key points (nose, left ear, right ear, neck, left hip, right hip, and tail base) of mouse were labeled on each frame. In total, 1,115 frames were labelled across 27 videos and used to train a ResNet-50–based neural network, with default parameters for 1,030,000 training iterations. With the trained network, the coordinates of key points in each frame of every video were estimated. The speed was computed as the change in the mouse's centroid based on the seven key points across two consecutive

frames.[68] To assess the effects of optogenetic V1 stimulation on these behaviors, the amplitude (eye movement, whisker movement, EMG power, and movement speed) was measured as the average between 0 and 2 s after laser onset after subtracting the baseline period (0 to 2 s before laser onset).

fUSi data processing and analysis

fUSi was performed as described previously.[11,12] Briefly, the ultrasound transducer (Verasonics, L22–14v) contained a linear array of 128 ultrasound emitters/receivers and emitted plane waves (15 MHz, 2 cycles) in five different angles (−6°, −3°, 0°, 3°, 6°). The echoes from each plane wave were acquired with the receivers and adjusted with a time–gain compensation to account for the attenuation of ultrasound signals with depth (exponential amplification of 1 dB/mm). This process generated a single emit–receive image ('B-mode image') for each angle and was applied three times for averaging, and then the 15 individual B-mode images were combined (2 ms, 500 Hz) to get a higher quality compound B-mode image. 500 compound B-mode images were acquired per second (1 Hz) to generate a functional ultrasound image. Blood cells flowing inside the vessels scatter back and shift the frequency of the emitted waves (Doppler effect). Such shifts were measured and extracted in real-time by a HPC workstation for real-time GP-GPU processing (fUSi HPC module, AUTC, Estonia). Each block of 500 images was processed using a singular–value–decomposition–based spatiotemporal filtering and high–pass temporal filtering (cut-off frequency: 20 Hz) to separate tissue signal from blood signal to obtain a final Power Doppler image exhibiting CBV in the whole imaging plane. Functional ultrasound images were semi-automatically aligned to a vascular atlas with Allen common coordinate framework (CCF) labels,[10,69] yielding Allen CCF labels for each functional ultrasound image voxel (50 x 50 x 50 μm^3).

The V1-evoked hemodynamic responses were calculated as ΔCBV/CBV, where CBV was the hemodynamic signal averaged over 5 s immediately before laser stimulation and ΔCBV was the signal at each time point minus the average. The hemodynamic signals were converted to z-scores based on the mean and standard deviation of the entire imaging session. The response amplitude was measured as the average between 0 and 7 s after laser onset after subtracting the baseline period (0 to 2 s before laser onset).

To find trials with matched delta power before and after CNO injection in the experiments with hM3Dq-mediated activation of basal forebrain cholinergic neurons, we first calculated the mean delta power during the entire imaging period before CNO injection; the delta power of individual trials was normalized to this mean. For each trial before CNO injection, we searched for a trial after CNO injection with <10% difference in delta power.

Fiber photometry data analysis

The 405-nm channel was used to correct nonspecific, calcium-independent changes in fluorescence, e.g., movement artifacts. Each channel (465-nm and 405-nm) was first fit with a single exponential to remove the baseline change due to bleaching. The 405-nm signal was then fit to the 465-nm signal using a least-squares linear fit method[70] and then subtracted from the 465-nm signal. The resulting signals were then converted to z-scores based on the mean and standard deviation of the entire imaging session. The response amplitude was computed as the average between 0 and 2 s after laser onset after subtracting the baseline period (0 to 2 s before laser onset).

Two-photon imaging data analysis

Data preprocessing was performed as described previously.[71] Briefly, time series of calcium activity images were motion corrected with Inscopix Data Processing software. Regions of interest (ROIs) corresponding to identifiable cell bodies were selected using the SD projection of the motion-corrected video using ImageJ[72] and a pixel-wise activity map.[73] The pixels within each ROI were averaged to create a fluorescence time series. The baseline fluorescence of the ROI (F0) was estimated as the eighth percentile[74] of the fluorescence in a ±60-s window and was used to calculate ΔF/F. A neuron was considered stimulus-responsive if the amplitude, calculated as the averaged ΔF/F between 0 and 5 s after laser onset after subtracting the baseline period (0 to 2 s before laser onset), was found to be statistically significant[75] during either wakefulness or NREM sleep.

Immunohistochemistry and fluorescence *in situ* hybridization (FISH)

Mice were deeply anesthetized and transcardially perfused using PBS followed by 4% paraformaldehyde in PBS. Brains were post–fixed in 4% paraformaldehyde for 24–48 h and stored in 30% sucrose in PBS solution for 48 h for cryoprotection. After embedding and freezing, brains were sectioned into 30 μm (for FISH) or 50 μm coronal slices using a cryostat (Leica). For immunohistochemistry, brain slices were washed using PBS three times, permeabilized using PBST (0.3% Triton X-100 in PBS) for 30 min, and then incubated with blocking solution (5% normal goat serum or normal donkey serum in PBST) for 1 h, followed by primary antibody incubation overnight at 4 °C using anti-GFP (GFP-1020, Aves Labs, 1:500). The next day, slices were washed three times with PBS, incubated with the secondary antibody (R37118, Alexa Fluor 488 donkey anti-chicken IgG, Jackson ImmunoResearch,1:500) for 2 h. FISH was done using RNAscope assays according to the manufacturer's instructions (Advanced Cell Diagnostics). Fluorescence images were taken using a high-throughput slide scanner (Hamamatsu, Nanozoomer 2.0–RS) and a fluorescence microscope (Keyence, BZ–X710).

QUANTIFICATION AND STATISTICAL ANALYSIS

For statistical analyses, each mouse was considered a unit. To measure activity propagation in different brain states, we conducted 2-3 imaging sessions per mouse, with each session encompassing multiple epochs of both NREM sleep and wakefulness. For each mouse, the data were first averaged across all trials within the same brain state in each session and then averaged across sessions; all sessions were included. Statistical analyses were performed using MATLAB and GraphPad Prism. One–way ANOVA with Tukey correction was used for comparisons of CBV or calcium activity across wakefulness, NREM and REM states. Two-way ANOVA with repeated measures followed by Bonferroni post-hoc test was used for changes in brain states after chemogenetic manipulation. Paired or unpaired t test was used for changes in activity between different treatments (saline vs. CNO, hM3Dq vs. hM4Di) in chemogenetic experiments. Full statistical analyses are described in the main text and figure legends.

Supplemental figures

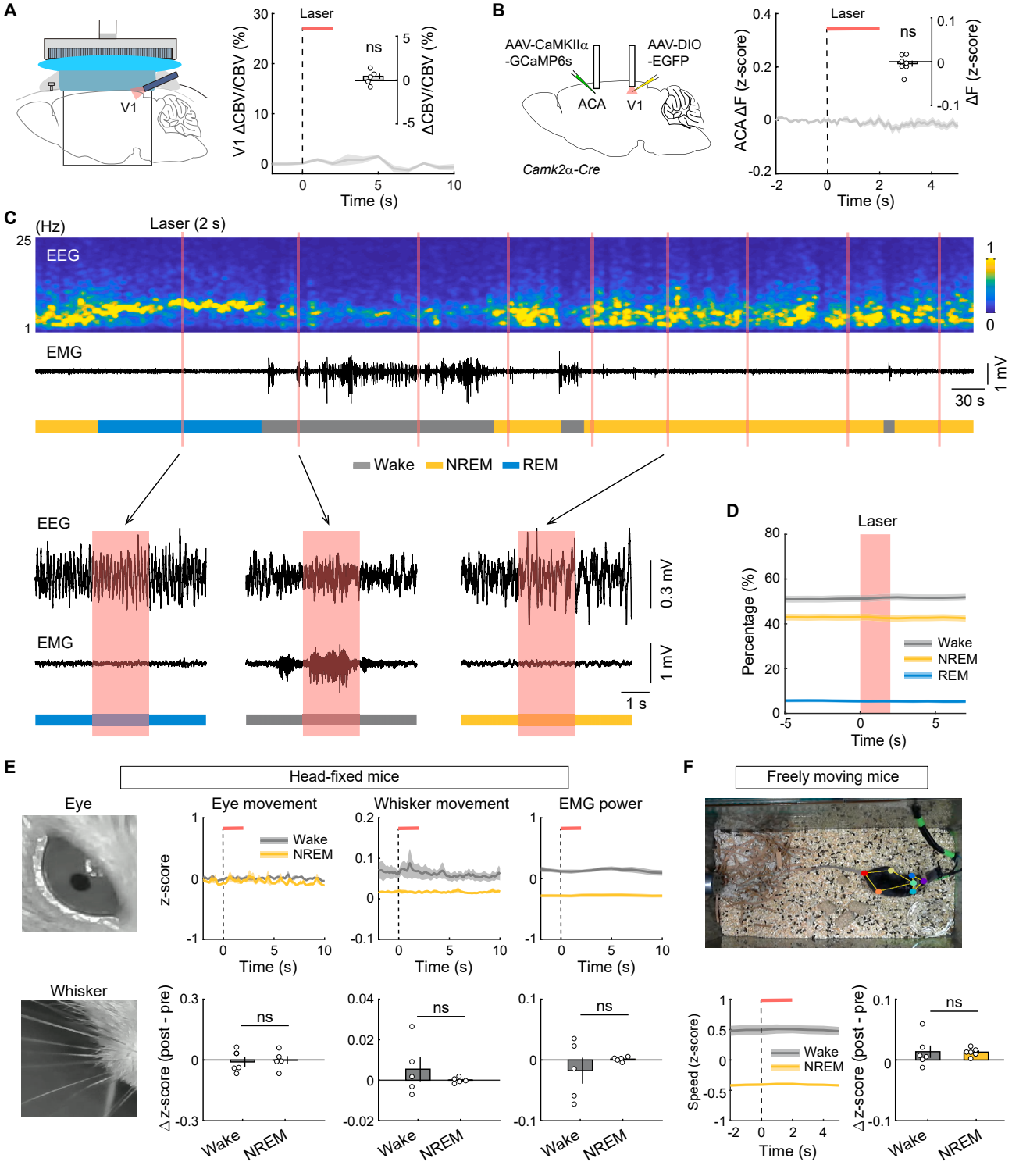

(legend on next page)

Figure S1. Effects of laser stimulation in V1, related to Figures 1 and 2

(A) Laser stimulation in mice not expressing ReaChR does not induce CBV responses. (Left) Schematic of the experiments. (Right) Laser-evoked CBV signals in V1 averaged across mice without ReaChR (n = 5 mice). Baseline signal was subtracted for each trial before averaging. Horizontal red bar, laser stimulation. Inset, summary of V1 response amplitudes calculated as the averaged CBV signals between 0 and 7 s after laser onset. Each circle represents one mouse ($p = 0.27$, two-tailed paired t test). Shading, ±SEM.

(B) Laser stimulation in V1 expressing EGFP evoked no calcium response in ACA. (Left) Schematic of the experiments. (Right) Laser-evoked calcium signals in ACA pyramidal neurons averaged across mice (n = 7 mice). Baseline signal was subtracted for each trial before averaging. Inset, summary of ACA response amplitudes calculated as the calcium signals averaged between 0 and 2 s after laser onset. Each circle represents one mouse ($p = 0.56$, two-tailed paired t test). Shading, ±SEM.

(C) EEG power spectrogram (recorded over the frontal cortical area), EMG, and laser stimulation in an example session with multiple sleep and wake episodes (color coded). Several laser trials (indicated by arrows) are shown at an expanded timescale.

(D) Percentage of time in wake, NREM, or REM state before, during, and after the 2 s laser stimulation. Shading, 95% confidence intervals. No significant change in brain states was observed.

(E) Eye and whisker movements and EMG power in head-fixed mice (n = 5 mice). (Left) Example images of a mouse's eye and whiskers. (Top right) Effects of laser on eye and whisker movements and EMG power during wakefulness and NREM sleep averaged across mice. (Bottom right) Summary of difference between the signal averaged between 0 and 2 s after laser onset and that between 0 and 2 s before laser onset. Each point represents one mouse. Eye movement, $p = 0.84$; whisker movement, $p = 0.42$; EMG power, $p = 0.45$ (two-tailed paired t test). Horizontal red bar, laser stimulation. Shading, ±SEM.

(F) Movement speed in freely moving mice (n = 6 mice). (Top) An example image of a freely moving mouse labeled by DeepLabCut. (Bottom left) Effects of laser on movement speed during wakefulness and NREM sleep averaged across mice. (Bottom right) Summary of difference between the speed averaged between 0 and 2 s after laser onset and that between 0 and 2 s before laser onset. Each point represents one mouse ($p = 0.95$, two-tailed paired t test). Horizontal red bar, laser stimulation. Shading, ±SEM.

Bar and error bar, mean ± SEM. *$p < 0.05$; **$p < 0.01$; ***$p < 0.001$; ns, not significant.

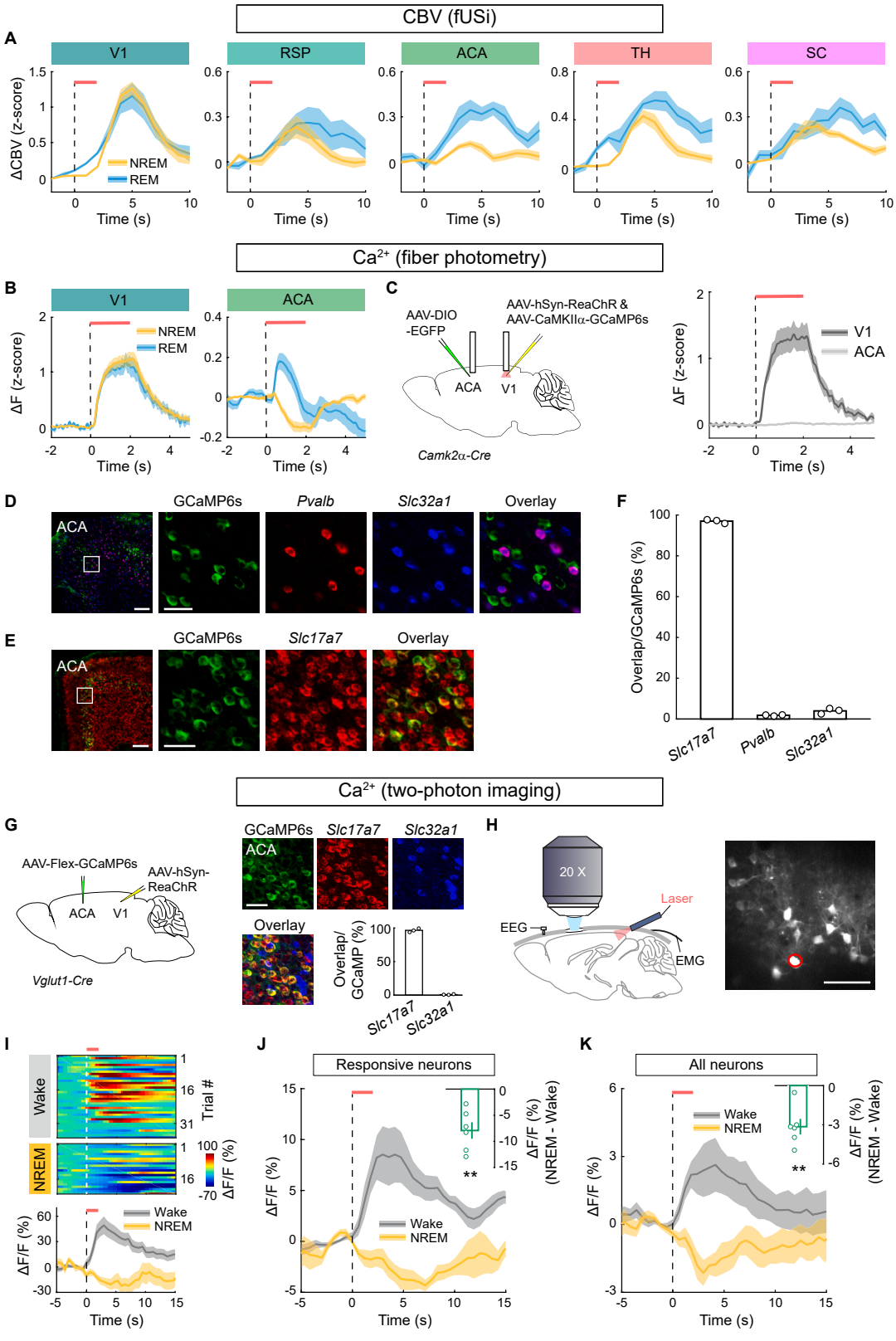

(legend on next page)

Figure S2. V1-evoked responses during REM sleep, histology data, and two-photon imaging, related to Figures 1 and 2

(A) V1-evoked CBV responses in several brain regions during NREM and REM sleep (V1, TH, n = 8 mice; RSP, SC, n = 5 mice; ACA, n = 13 mice). Baseline activity was subtracted for each trial before averaging. Horizontal red bar, laser stimulation.

(B) V1-evoked calcium responses from V1 and ACA pyramidal neurons during NREM and REM sleep (n = 12 mice). Baseline activity was subtracted for each trial before averaging. Horizontal red bar, laser stimulation.

(C) ACA signals showed no contamination from activity of V1 terminals. (Left) Schematic of the experiment with GCaMP6s expressed in V1 neurons and EGFP expressed in ACA neurons. (Right) Laser-evoked responses in V1 and ACA (n = 5 mice). Baseline signal was subtracted for each trial before averaging. Horizontal red bar, laser stimulation.

(D) Overlap between GCaMP-labeled neurons (green), *Pvalb* (red), and *Slc32a1* (encoding vesicular GABA transporter VGAT, blue) mRNA detected by fluorescence *in situ* hybridization (FISH) in the ACA. The region in the white box in the left panel (scale bars, 200 μm) is enlarged. Scale bars, 50 μm.

(E) Overlap between GCaMP-labeled neurons (green) and *Slc17a7* (encoding vesicular glutamate transporter VLGUT1, red) mRNA in the ACA. The region in the white box in the left panel (scale bars, 200 μm) is enlarged. Scale bars, 50 μm.

(F) Percentages of GCaMP-labeled neurons in the ACA that express *Slc17a7* (n = 3 mice), *Pvalb* (n = 3 mice), or *Slc32a1* (n = 3 mice). Each circle represents one mouse.

(G) (Left) Schematic of virus injection for two-photon imaging. (Right) Overlap between GCaMP-labeled neurons (green), *Slc17a7* (red), and *Slc32a1* (blue) mRNA in the ACA. Each circle represents one mouse (n = 3 mice). Scale bars, 50 μm.

(H) Two-photon calcium imaging in head-fixed mice. (Left) Schematic of the experiments. (Right) Example image of GCaMP-labeled neurons. An example neuron shown in (I) is indicated by a red circle. Scale bars, 50 μm.

(I) Laser-evoked calcium responses of an example neuron in (H). (Top) ACA pyramidal neuron calcium activity evoked by optogenetic V1 stimulation in an example session, with trials during wakefulness and NREM sleep. (Bottom) Calcium responses averaged across all trials. Baseline signal was subtracted for each trial before averaging. Horizontal red bar, laser stimulation.

(J) Laser-evoked calcium responses from responsive neurons (n = 171 neurons from 6 mice) averaged across all mice. A neuron was considered stimulus-responsive if the amplitude, calculated as the averaged ΔF/F between 0 and 5 s after laser onset after subtracting the baseline period (0 to 2 s before laser onset), was found to be statistically significant during either wakefulness or NREM sleep. Inset, difference in averaged response amplitudes between NREM sleep and wakefulness for each mouse ($p = 0.004$, two-tailed paired t test). Baseline signal was subtracted for each trial before averaging. Horizontal red bar, laser stimulation.

(K) Similar to (J), but for all neurons (n = 1,075 neurons from 6 mice, $p = 0.0033$).

Bar and error bar, mean ± SEM. Shading, ±SEM. *$p < 0.05$; **$p < 0.01$; ***$p < 0.001$; ns, not significant.

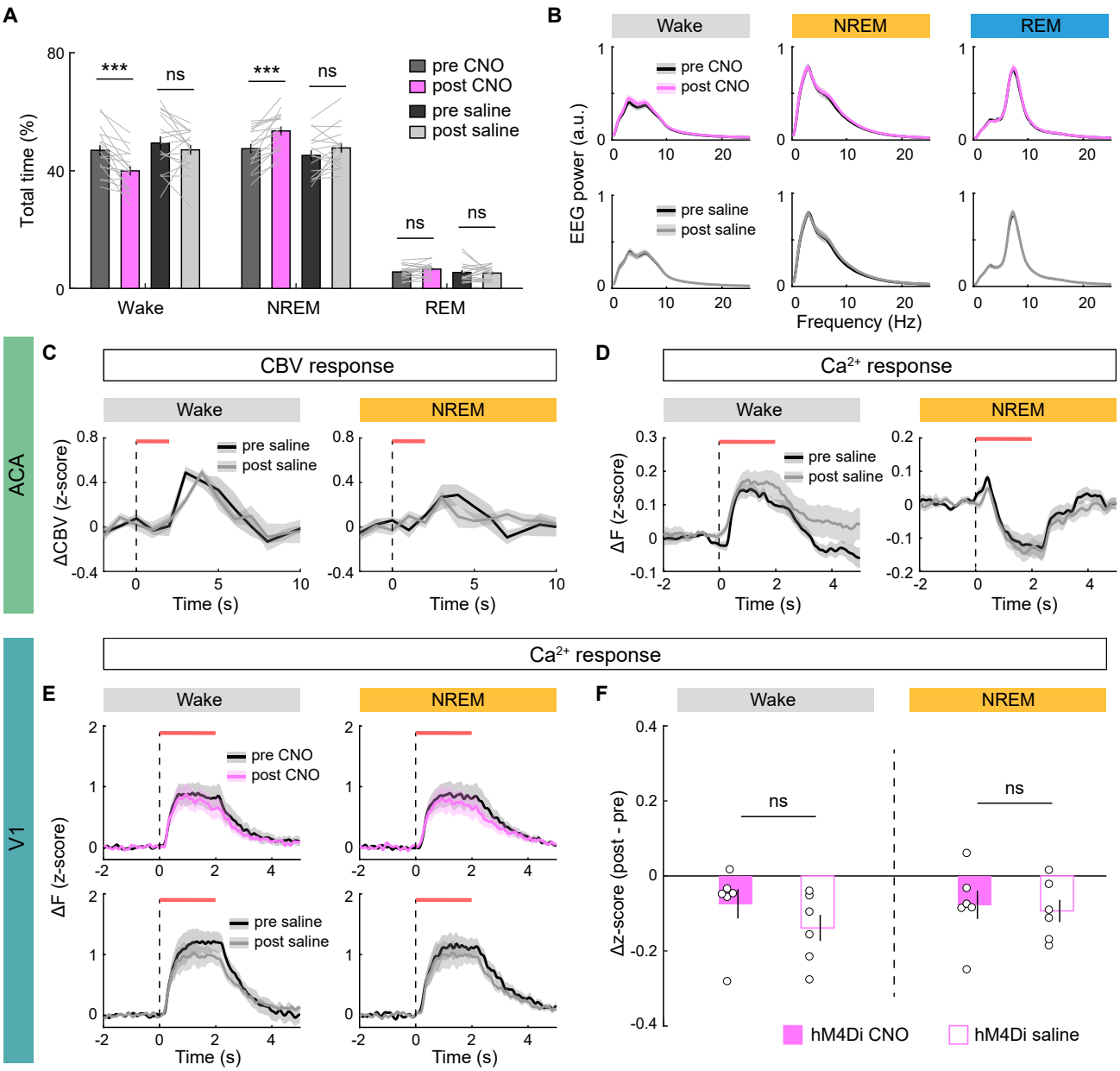

Figure S3. Effects of chemogenetic inactivation of basal forebrain cholinergic neurons on brain states and laser-evoked V1 pyramidal neuron calcium activity, and saline control experiment, related to Figure 3

(A) Total time in wake, NREM, or REM state before and after CNO or saline injection in mice expressing hM4Di in cholinergic neurons (n = 17 mice). Effect of CNO: wake, p = 0.0007; NREM, p = 0.0001; REM, p = 0.41. Effect of saline: wake, p = 0.39; NREM, p = 0.12; REM, p > 0.99. CNO vs. saline effects (difference before and after injection): wake, p = 0.21; NREM, p = 0.21; REM, p = 0.83 (two-way ANOVA with repeated measures followed by Bonferroni post hoc test).

(B) EEG power spectra in each brain state are very similar before and after CNO or saline injection.

(C) V1-evoked ACA CBV responses before and after saline injection during wakefulness (left) or NREM sleep (right) (n = 5 mice). Baseline activity was subtracted for each trial before averaging. Horizontal red bar, laser stimulation.

(D) Similar to (C), but for ACA pyramidal neuron calcium activity (n = 12 mice).

(E) Optogenetically evoked V1 pyramidal neuron calcium activity before (black) and after (colored) CNO (top) or saline (bottom) injection during wakefulness (left) or NREM sleep (right), averaged across mice expressing hM4Di in cholinergic neurons. Baseline activity was subtracted for each trial before averaging. Horizontal red bar, laser stimulation. The slight amplitude reduction after saline injection is likely due to bleaching.

(F) Summary of amplitude difference before and after CNO (filled) or saline (unfilled) injection. Each point represents one mouse.

Bar and error bar, mean ± SEM. Shading, ±SEM. *p < 0.05; **p < 0.01; ***p < 0.001; ns, not significant.

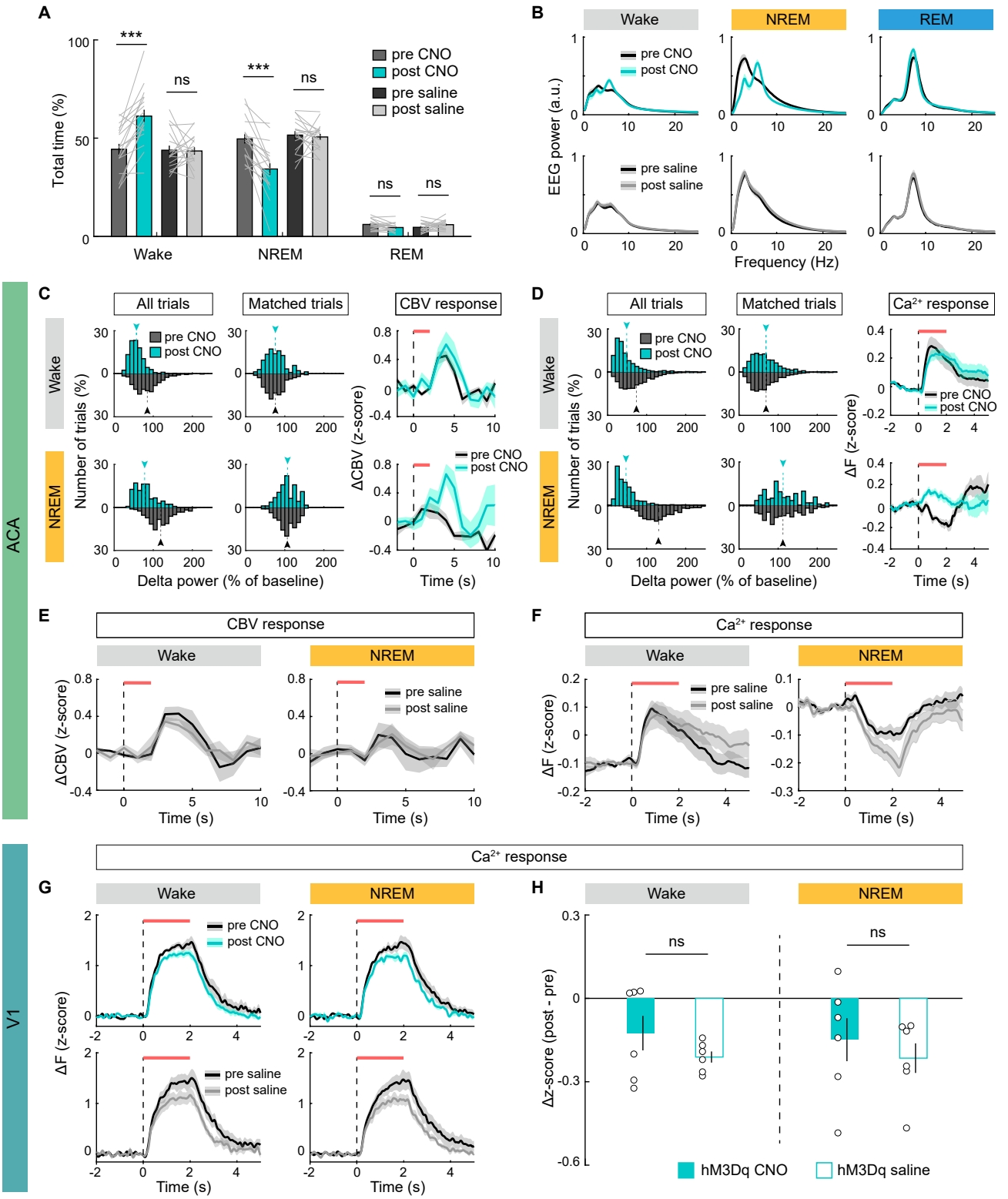

(legend on next page)

Figure S4. Effects of chemogenetic activation of basal forebrain cholinergic neurons on brain states and laser-evoked V1 pyramidal neuron calcium activity, and saline control experiment, related to Figure 4

(A) Total time in wake, NREM, or REM state before and after CNO or saline injection in mice expressing hM3Dq in cholinergic neurons (n = 18 mice). Effect of CNO: wake, $p < 10^{-4}$; NREM, $p < 10^{-4}$; REM, $p = 0.12$. Effect of saline: wake, $p > 0.99$; NREM, $p > 0.99$; REM, $p = 0.2$. CNO vs. saline effects (difference before and after injection): wake, $p = 0.0012$; NREM, $p = 0.002$; REM, $p = 0.047$ (two-way ANOVA with repeated measures followed by Bonferroni post hoc test).

(B) EEG power spectra in each brain state before and after CNO or saline injection. CNO but not saline injection caused a decrease in delta power.

(C) Comparison of ACA CBV responses in trials with matched EEG delta power before and after CNO injection. The baseline delta power was computed by averaging across the imaging period before CNO injection, and the delta power of individual trials, both before and after CNO injection, was normalized by this baseline. To find trials with matched delta power before and after CNO injection, for each trial before CNO injection, we searched for a trial after CNO injection with <10% difference in delta power and took it as a matched trial. Left, distribution of delta power in all trials (vertical dashed line and arrowhead indicate mean of each distribution); middle, distribution of delta power in matched trials (with very similar mean values); right, V1-evoked ACA CBV responses in matched trials before and after CNO injection during wakefulness (top) or NREM sleep (bottom). Responses were still enhanced during NREM sleep. Horizontal red bar, laser stimulation. Baseline activity was subtracted for each trial before averaging.

(D) Similar to (C), but for ACA pyramidal neuron calcium activity. Responses were still enhanced during NREM sleep.

(E) V1-evoked ACA CBV responses before and after saline injection during wakefulness (left) or NREM sleep (right) (n = 5 mice). Baseline activity was subtracted for each trial before averaging. Horizontal red bar, laser stimulation.

(F) Similar to (E), but for ACA pyramidal neuron calcium activity (n = 13 mice).

(G) Optogenetically evoked V1 pyramidal neuron calcium activity before (black) and after (colored) CNO (top) or saline (bottom) injection during wakefulness (left) or NREM sleep (right), averaged across mice expressing hM3Dq in cholinergic neurons. Baseline activity was subtracted for each trial before averaging. Horizontal red bar, laser stimulation. The slight amplitude reduction after saline injection is likely due to bleaching.

(H) Summary of amplitude difference in the V1 before and after CNO (filled) or saline (unfilled) injection. Each point represents one mouse.

Bar and error bar, mean ± SEM. Shading, ±SEM. *$p < 0.05$; **$p < 0.01$; ***$p < 0.001$; ns, not significant.

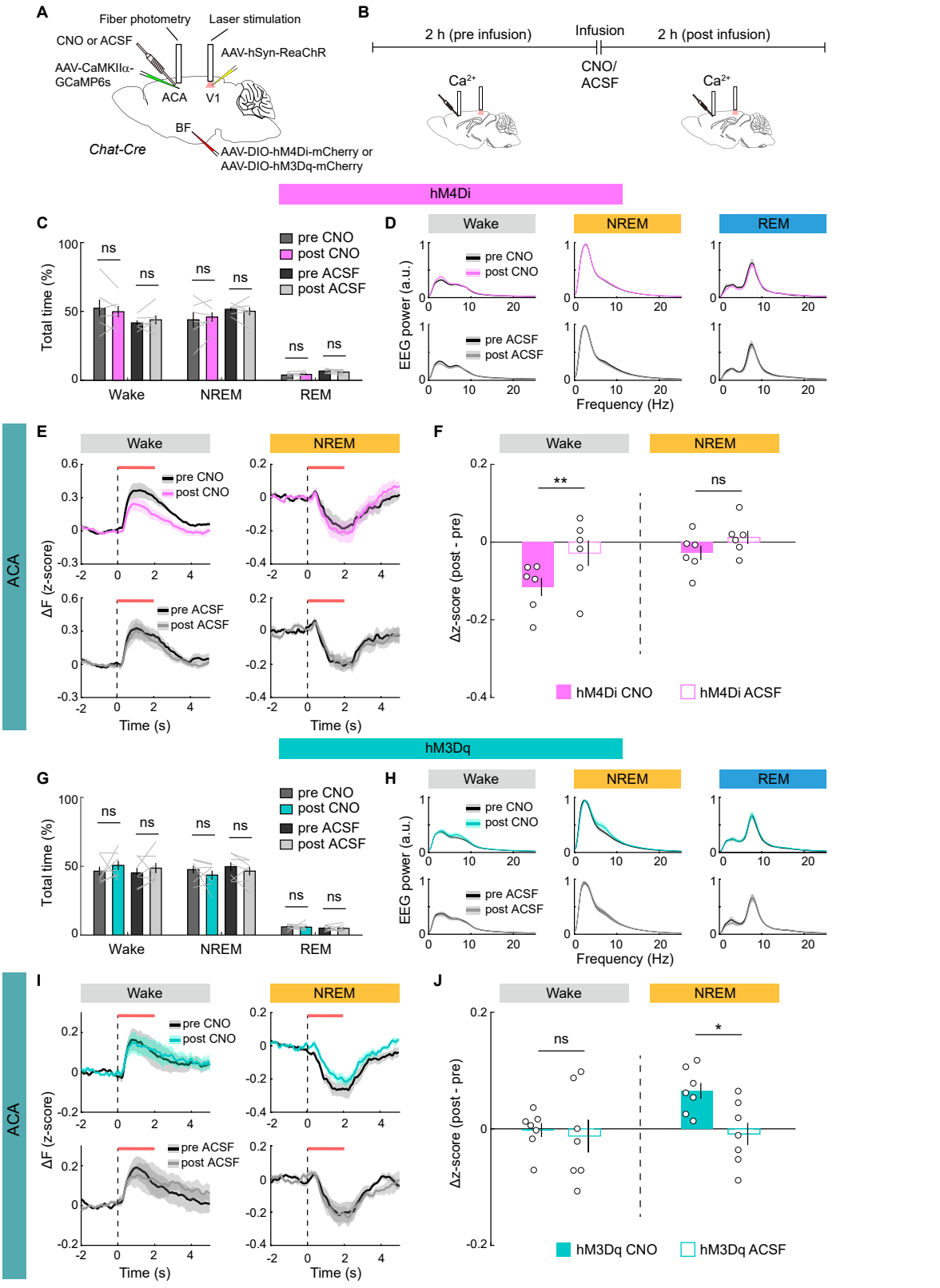

(legend on next page)

Figure S5. Effects of local manipulation of basal forebrain cholinergic input to the ACA, related to Figures 3 and 4

(A) Schematic of local manipulation of basal forebrain cholinergic input to the ACA.

(B) Schematic for experimental session with local chemogenetic manipulation.

(C) Total time in wake, NREM, or REM state before and after CNO or artificial cerebrospinal fluid (ACSF) infusion in mice expressing hM4Di in basal forebrain cholinergic neurons (n = 6 mice). Effect of CNO: wake, $p = 0.91$; NREM, $p > 0.99$; REM, $p > 0.99$. Effect of ACSF: wake, $p = 0.99$; NREM, $p > 0.99$; REM, $p = 0.58$. CNO vs. ACSF effects (difference before and after injection): wake, $p = 0.96$; NREM, $p > 0.99$; REM, $p = 0.73$ (two-way ANOVA with repeated measures followed by Bonferroni post hoc test).

(D) EEG power spectra in each brain state are similar before and after CNO or ACSF infusion.

(E) V1-evoked ACA pyramidal neuron calcium activity before (black) and after (colored) CNO (top) or ACSF (bottom) infusion during wakefulness (left) or NREM sleep (right), averaged across mice expressing hM4Di in cholinergic neurons. Baseline activity was subtracted for each trial before averaging. Horizontal red bar, laser stimulation.

(F) Summary of amplitude difference before and after CNO (filled) or ACSF (unfilled) infusion. Each point represents one mouse.

(G–J) Similar to (C)–(F), but for mice expressing hM4Dq in basal forebrain cholinergic neurons (n = 7 mice). In (G), effect of CNO: wake, $p = 0.76$; NREM, $p = 0.59$; REM, $p > 0.99$. Effect of ACSF: wake, $p = 0.95$; NREM, $p = 0.80$; REM, $p > 0.99$. CNO vs. ACSF effects (difference before and after injection): wake, $p > 0.99$; NREM, $p > 0.99$; REM, $p > 0.99$.

Bar and error bar, mean ± SEM. Shading, ±SEM. *$p < 0.05$; **$p < 0.01$; ***$p < 0.001$; ns, not significant.

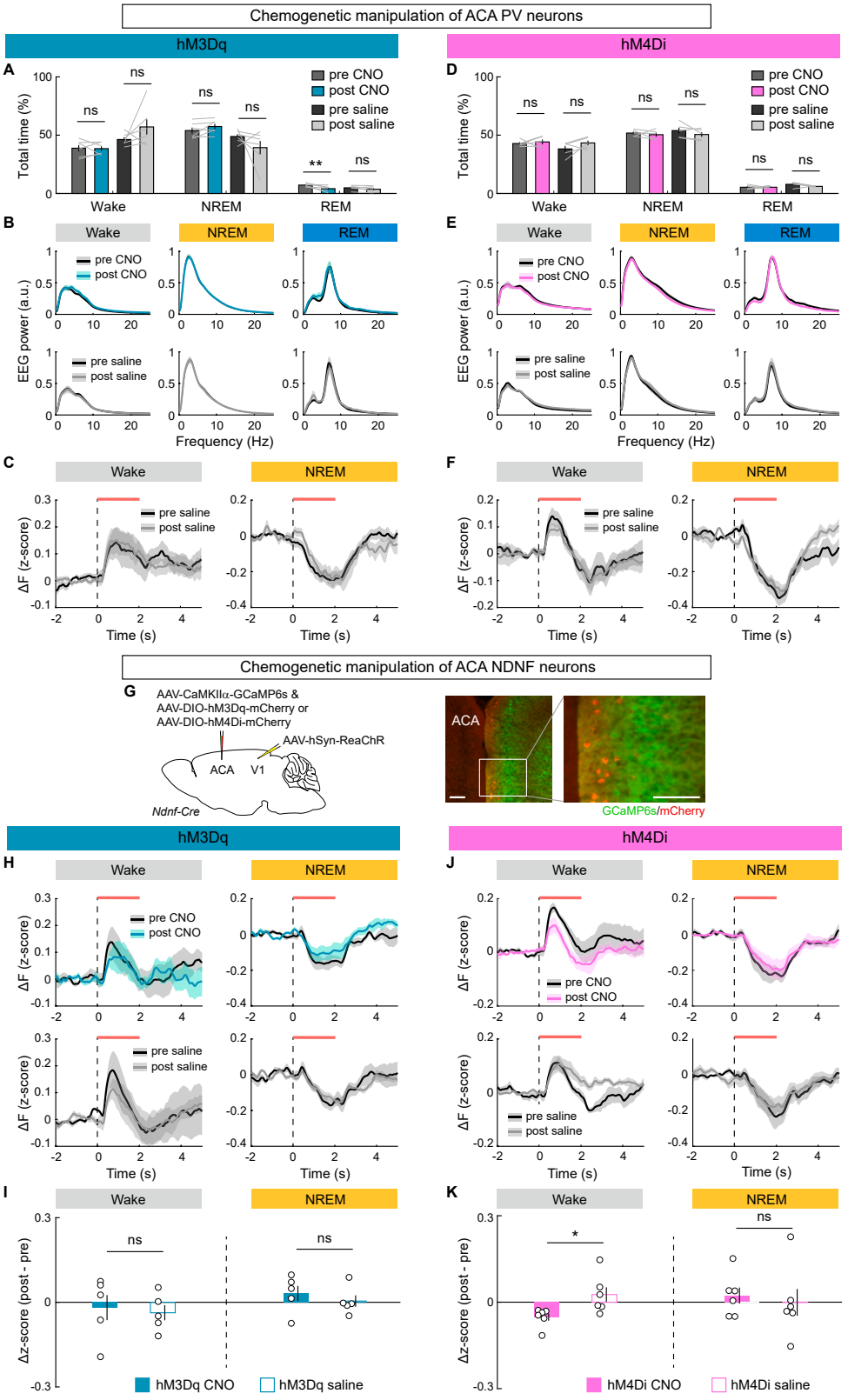

(legend on next page)

Figure S6. Effects of chemogenetic manipulation of ACA PV neurons and NDNF neurons, related to Figure 6

(A) Total time in wake, NREM, or REM state before and after CNO or saline injection in mice expressing hM3Dq in ACA PV neurons (n = 6 mice). Effect of CNO: wake, $p > 0.99$; NREM, $p > 0.99$; REM, $p = 0.0048$. Effect of saline: wake, $p = 0.2$; NREM, $p = 0.26$; REM, $p = 0.27$. CNO vs. saline effects (difference before and after injection): wake, $p = 0.7$; NREM, $p = 0.49$; REM, $p = 0.38$ (two-way ANOVA with repeated measures followed by Bonferroni post hoc test).

(B) EEG power spectra in each brain state are very similar before and after CNO or saline injection.

(C) V1-evoked ACA pyramidal neuron calcium responses before and after saline injection during wakefulness (left) and NREM sleep (sleep). Baseline activity was subtracted for each trial before averaging (n = 6 mice). Horizontal red bar, laser stimulation.

(D–F) Similar to (A)–(C), but for mice expressing hM4Di in ACA PV neurons (n = 5 mice). In (D), effect of CNO: wake, $p > 0.99$; NREM, $p > 0.99$; REM, $p > 0.99$. Effect of saline: wake, $p = 0.28$; NREM, $p = 0.38$; REM, $p = 0.37$. CNO vs. saline effects: wake, $p > 0.99$; NREM, $p > 0.99$; REM, $p = 0.97$.

(G) (Left) Schematic of chemogenetic manipulation of ACA NDNF neurons and calcium imaging of ACA pyramidal neuron activity. (Right) Expression of GCaMP6s (green) in pyramidal neurons and mCherry in NDNF neurons (red) in the ACA. The region in white box is enlarged. Scale bars, 100 μm.

(H) V1-evoked ACA pyramidal neuron calcium activity before (black) and after (colored) CNO (top) or saline (bottom) injection during wakefulness (left) or NREM sleep (right), averaged across mice expressing hM3Dq in ACA NDNF neurons. Baseline activity was subtracted for each trial before averaging. Horizontal red bar, laser stimulation.

(I) Summary of amplitude difference in the ACA before and after CNO (filled) or saline (unfilled) injection. Each point represents one mouse.

(J and K) Similar to (H) and (I), but for mice expressing hM4Di in ACA NDNF neurons.

Bar and error bar, mean ± SEM. Shading, ±SEM. *$p < 0.05$; **$p < 0.01$; ***$p < 0.001$; ns, not significant.